Earth's earliest global glaciation? Geochronology and carbonate geochemistry of the Polisarka Sedimentary Formation, Kola Peninsula, Russia

A.T. Brasier[1*], A.P. Martin[2+], V.A. Melezhik[3,4], A.R. Prave[5], D.J. Condon[2], A.E. Fallick[6] and FAR-DEEP Scientists

1# Faculty of Earth and Life Sciences, Vrije Universiteit Amsterdam, De Boelelaan 1085, 1081HV Amsterdam

2 NERC Isotope Geosciences Laboratory, British Geological Survey, Environmental Science Centre, Keyworth, UK. NG12 5GG

3 Geological Survey of Norway, Postboks 6315 Slupen, NO-7491 Trondheim, Norway

4 Centre for Geobiology, University of Bergen, Postboks 7803, NO-5020 Bergen, Norway

5 Department of Earth and Environmental Sciences, University of St Andrews, St Andrews KY16 9AL, Scotland, UK

6 Scottish Universities Environmental Research Centre, Rankine Avenue, East Kilbride, Scotland. G75 0QF

*corresponding author (a.brasier@abdn.ac.uk)

+ present address: GNS Science, Private Bag 1930, Dunedin, New Zealand

present address: Department of Geology and Petroleum Geology, Meston Building, University of Aberdeen, Scotland, UK. AB24 3UE.

Research highlights:

ICDP FAR-DEEP Hole 3A targeted Palaeoproterozoic diamictites of the Polisarka Sedimentary Formation of Russian Fennoscandia ► Zircon U-Pb dating of a tuff above the diamictites yielded a minimum age of 2434 Ma for the diamictites ► This new U-Pb age constrains the onset of the

Palaeoproterozoic glaciation in Fennoscandia to between ca. 2430 and ca. 2440 Ma suggesting it was one of the earliest Palaeoproterozoic glaciations ► carbonate $\delta^{13}C$ analyses of carbonate rocks below the diamictites revealed two excursions to ca. -5‰ ► the origins of these excursions are carefully considered

Abstract

As part of the International Continental Scientific Drilling Program's Fennoscandian Arctic Russia – Drilling Early Earth Project (ICDP FAR-DEEP), Palaeoproterozoic diamictic and associated rocks were targeted and recovered in Hole 3A on the Kola Penninsula of NW Russia. In addition to the diamictites, carbonate sedimentary rocks and volcanic ash layers (all metamorphosed to greenschist grade) were encountered. Sedimentology and geochemistry suggest deposition of the diamictites in an open-marine aragonite-precipitating environment. Sampling of the core and of outcrops from the same geographical area yielded a number of zircons for analyses, the majority of which were inherited in nature. However a tuff at 20.01 m core depth yielded zircons dated at 2434 ± 1.2 Ma (± 6.6 Myr including decay constant uncertainties) that we interpret a magmatic age. These data, combined with dates from underlying intrusions indicate deposition of the Polisarka Sedimentary Formation diamictites and underlying carbonates during an interval of time from ca. 2430 to 2440 Ma. The carbonate rocks, which likely originally included aragonitic limestones, were deposited mostly in a deep-water setting (i.e, below storm wave base) and occur below the diamictite. They record two inorganic carbon $\delta^{13}C$ excursions, from values of ca. 0‰ to minima of ca. -5.4‰, as the contact with the overlying diamictite is approached. Mg/Ca ratios correlate strongly with $\delta^{13}C$ in the sections containing the excursions ($n = 38$, $r = 0.85$), and combined with petrographic observations, this reflects that the first excursion was modified by secondary alteration and the second is recorded in resedimented dolostone clasts. It is tempting to speculate that these dolostone clasts were deposited in penecontemporaneous shallow-marine waters as the global glaciation began. In this scenario, their low $\delta^{13}C$ values might reflect input of oxidised atmospheric

methane to the ocean surface (and therefore the cause of the glaciation), while the majority of the ICDP FAR-DEEP Hole 3A carbonates record deeper-marine inorganic carbon $\delta^{13}C$. However this must be left as a hypothesis to be tested when further age-constrained contemporaneous pre-glacial carbonate sections are found.

Keywords:
Huronian-age glaciation; carbon isotopes; carbonate rocks; Palaeoproterozoic; Great Oxidation Event

Introduction

During the purported global glaciation episode(s) of the Palaeoproterozoic, ice extended from the poles to low latitudes at least once (e.g. Evans et al., 1997; Mertanen et al., 1999; Melezhik, 2006; Melezhik et al., 2013a; Hoffman, 2013). These early glaciations may have been as significant for biological and geological evolution as the 'Snowball Earth' episodes in the Neoproterozoic, a billion years later. Robust geochemical testing of proposed causes for severe climatic deterioration in the Palaeoproterozoic has been hindered by lack of suitable rock types in immediately pre-glacial sections.

Varied explanations for initiation of glaciation have included atmospheric CO_2 (greenhouse gas) drawdown resulting from enhanced chemical weathering of silicate rocks because of collisional tectonics (Young, 1991), rifting at low latitudes (e.g. Evans, 2003), and a combination of tectonic and environmental factors (Melezhik, 2006). These models implicitly require lengthy (million-year timescale) durations as they involve involve processes operating at rates of the geological rock cycle. These models do all permit repeat episodes of global freezing, as observed in the rock record. Another potential driver to consider is catastrophic and rapid oxidation of Earth's proposed early methane atmosphere (e.g. Kasting et al., 1983; Pavlov et al., 2000; Kopp et al., 2005; Papineau et

al., 2005; 2007). Here, the warming effect of a methane-rich atmosphere might have counteracted the relative weakness of the young Sun and a methane atmosphere was invoked to explain the relative lack of evidence for glaciation until the Palaeoproterozoic (Pavlov et al., 2000; see also corrections by Haqq-Misra et al., 2008). This state-of-affairs ended when atmospheric free oxygen first became widespread ca. 2.4 billion years ago (e.g. Pavlov et al., 2000; Kopp et al., 2005; Kasting, 2005; Melezhik, 2006; Haqq-Misra et al., 2008; Guo et al., 2009), the 'Great Oxidation Event' (GOE). Photochemical dissociation of ozone in the newly oxic atmosphere (with less free H_2) would have given rise to free OH^- radicals. These, in turn, could have reacted with methane to produce $CH_3 + H_2O$, as well as a series of short-lived organic molecules (Ravishankara, 1988), and, finally, bicarbonate ions. It has been estimated that the GOE would have shortened the lifetime of methane in the atmosphere from 10^5 to ~10^1 years (as found at present; Pavlov et al., 2003; Kasting, 2005). Although it now seems that methane alone would not have been a sufficiently strong greenhouse gas to keep the early Earth ice-free (e.g. Haqq-Misra et al., 2008), the latter authors concluded that loss of methane from the atmosphere was still a likely trigger for glaciations around 2.4 billion years ago. The methane oxidation hypothesis is testable because it implies a one-off, unrepeatable rapid transfer of a vast quantity of ^{13}C-depleted carbon from the atmosphere to the surface oceans as the trigger for the first Palaeoproterozoic glaciation. This likely would have been recorded in contemporaneous marine carbonate rocks, which is why Palaeoproterozoic carbonate rocks below diamictites recently discovered in Fennoscandian Russia are important. These were found in International Continental Drilling Program (ICDP) Fennoscandian Arctic Russia – Drilling Early Earth Project (FAR-DEEP) Hole 3A which targeted the Polisarka Sedimentary Formation of the Imandra-Varzuga Belt (Fig. 1). Stable isotopic analyses of these carbonates are reported here, with the aim of illuminating the cause of the glaciation. In addition, volcanic ash beds have been sampled for U-Pb dating of zircons to constrain the age of the diamictite-containing Polisarka Sedimentary Formation, thereby aiding global correlations and geologic context.

Geological setting

ICDP FAR-DEEP Hole 3A was drilled in the Imandra-Varzuga Greenstone Belt at latitude 67.4862N, longitude 34.5404E, between the 7th and 14th September 2007, to a total depth of 254.5 m (see Fig. 1). The target was the Palaeoproterozoic Polisarka Sedimentary Formation (Fig. 2), known from outcrop to contain diamictites (Fig. 3f) that could correlate with the Huronian diamictites of North America (Melezhik, 2013). Depths given in this manuscript are in metres composite depth (MCD).

The diamictite-containing Polisarka Sedimentary Formation is unconformably underlain by the Seidorechka Volcanic and Seidorechka Sedimentary formations, which in turn overly the Kuksha and Purnach formations (Fig. 2). The Kuksha Volcanic Formation lies unconformably on the Monchegorsk layered gabbro-norite pluton (Chashchin et al., 2008), and the Kuksha Sedimentary Formation seals eroded and faulted surfaces of the pluton (Melezhik, 2013; Melezhik et al. 2013a). Zircons from the Monche Pluton were radio-isotopically dated at 2504.4 ± 1.5 Ma (ID-TIMS $^{207}Pb/^{206}Pb$ weighted mean date; Amelin et al., 1995). In the mid- to upper-Seidorechka Formation, baddeleyite grains in a subvolcanic unit yield a 2442.2 ± 1.7 Ma age (ID-TIMS upper intercept date; Amelin et al., 1995). This unit is spatially and temporally associated with an intrusion (the Imandra lopolith) dated by U-Pb ID-TIMS at 2441 ± 1.6 Ma (ID-TIMS $^{207}Pb/^{206}Pb$ weighted mean date; Amelin et al., 1995).

In the western part of the Imandra-Varzuga Greenstone Belt, the Avarench locality is comprised of a komatiitic basalt – andesite – dacite – rhyolite association that is considered the lithostratigraphic equivalent of Strelna Group rocks, including the Kuksha and Seidorechka Formations. Zircons extracted from two samples of plagioclase and quartz dacitic metaporphyrites yield an age at 2429 ± 6.6 Ma (U-Pb zircon SHRIMP date; Vrevsky et al., 2010). This dated unit is considered to be the litho- and chrono-stratigraphic equivalent of the Seidorechka Volcanic Formation (e.g., Melezhik, 2013). The c. 2504 Ma age of the Monche Pluton is the most robust maximum age for the Imandra-

Varzuga belt succession, and provides one age constraint to the Polisarka Sedimentary Formation. However, if the interpretation of Amelin et al. (1995) that the subvolcanic (c. 2442 Ma) unit is a 'feeder' to the Seidorechka Volcanic Formation is correct, then the age of the spatially associated Imandra Lopolith (slightly younger than 2442Ma, at ca. 2441 Ma) can be taken as a maximum age for the Polisarka Sedimentary Formation.

Evidence for Palaeoproterozoic glaciation in the Fennoscandian region includes diamictites and dropstones of the Urkkavaara Formation (Sariolian group, Marmo and Ojakangas (1984)). There are known dropstones in sediments with varve-like laminations in the Polisarka Sedimentary Formation (Fig. 3f; Imandra-Varzuga Greenstone Belt; Melezhik et al., 2013b) and its stratigraphic equivalents in the Shambozero and Lekhta Greenstone Belts (cf. Negrutsa, 1984). None of these naturally exposed Fennoscandian sections are known to include a carbonate unit below the diamictite, so the discovery of such rocks in ICDP FAR-DEEP Hole 3A was serendipitous.

ICDP FAR-DEEP Hole 3A: stratigraphic and preservational context of the carbonates

The Polisarka Sedimentary Formation in ICDP FAR-DEEP Hole 3A is sandwiched between rhyodacites of the underlying Seidorechka Volcanic Formation and mafic komatiites of the overlying Polisarka Volcanic Formation. It was informally divided by Melezhik et al. (2013b) into a lower carbonate-rich Limestone member and an upper siliciclastic Greywacke-diamictite member. The contact between these members lies at around 123.8 m depth. The first thick diamictite bed occurs at around 114 m (Fig. 2). Three smaller diamictite units have been documented in the Limestone member. The first out-sized clast associated with deformed underlying laminae occurs at 183.2m but its origin as a potential dropstone is tempered by the fact that variably developed tectonic shearing is present in ICDP FAR-DEEP Hole 3A. Clasts and dropstones (Fig. 3a; 3g) are commonly tectonically flattened or exhibit sigmoidal morphologies, with their long axes parallel to bedding and shearing (Fig. 3a). In the Limestone member, millimetre-scale laminations comprising

157 laterally discontinuous layers of carbonate alternating with layers of siltstone might reflect an
158 original sedimentary texture (Fig. 3b; Melezhik et al., 2013b), but bedding-parallel shearing can
159 generate transposed bedding resulting in a metamorphic-related ‘pseudo-lamination’. This
160 greenschist facies metamorphism complicates the interpretation of depositional environments here,
161 but sedimentary features can be distinguished in low-strain zones.
162
163 On a broad scale, Melezhik et al. (2013b) suggested that fine compositional laminae and lack of
164 traction-bedded structures indicate a relatively deep-water setting (below effective storm and
165 fairweather wave base) for the Limestone member (Fig. 2). They suggested that exotic and faceted
166 diamictite clasts that in places pierce compositional layering indicate a glacio-marine origin for the
167 Greywacke-diamictite member. The transition from the Limestone member to the overlying
168 Greywacke-diamictite member is one of siliciclastic upward coarsening over several metres, and the
169 contact itself is marked by a sharp-based medium to coarse-grained laminated arkosic sandstone.
170 These relationships are consistent with glacio-eustatic sea-level fall, with the arkosic bed
171 representing a consequent base level incision and basinward facies shift. It is difficult to assess the
172 water depth in which the glacial diamictites were deposited, but we assume on the basis of sequence
173 stratigraphic principles that they were deposited in shallower settings than the carbonate rocks.
174
175 Melezhik et al. (2013b) briefly described several igneous bodies encountered in the Limestone
176 member (Fig. 2). These include a thin alkaline ultramafic body (225.15 to 225.97 m) that is best
177 interpreted as a dyke belonging to the Palaeozoic alkaline province of the Kola Peninsula; 0.2 to 4m
178 thick mafic bodies that have been interpreted as Palaeoproterozoic lava flows (212 to 189 m); and a
179 44 m thick massive ultramafic peridotite (175.68 to 131.17 m). Diagnostic features that would allow
180 the latter to be ascribed as either intrusive or extrusive seem to be lacking. Igneous bodies including
181 komatiites are also encountered above the diamictite sediments (Fig. 2).
182

Methodology: stable isotopes and elemental geochemistry

Fifteen bulk rock archive samples were initially taken from the cores, spaced ca. 1 to 5 m apart. These archive samples were powdered for geochemical analysis to give 'bulk rock' elemental (XRF and ICP-AES) and stable isotopic (carbonate O and C) data. A further 115 samples were later taken with a spacing of 15 cm through the most carbonate-rich sections. These were also crushed for similar geochemical analysis. A further phase of sampling was undertaken using a hand-drill to target specific carbonate fabrics, and powders obtained were used exclusively for carbonate stable isotope analyses.

Concentrations of SiO_2, Fe_2O_3, CaO and MgO were determined by X-ray fluorescence spectrometry at the Geological Survey of Norway (NGU), Trondheim, using a PANalztical Axios at 4 kW. The precision (1σ) was typically around 2% of the major oxides present. Concentrations of elements in acid-soluble components were determined by inductively coupled plasma-atomic emission spectrometry (ICP-AES) at NGU using a Thermo Jarrell Ash ICP 61 instrument, with detection limits for Fe, Mg, Ca, Mn and Sr being 5, 100, 200, 0.2 and 2 μg/g, respectively. The precision (1σ), including element extraction, was ±10%. Total organic carbon (TOC) and total carbon (TC) were measured at NGU using standard analytical procedures: the TC and TOC content were determined from acid-washed material via sealed tube combustion using a Leco SC-444 instrument with a total analytical uncertainty of 15%. All analysed samples showed the TOC content below a detection limit of 0.1%

For bulk carbonate O and C isotopes, ca. 1 mg powders were dissolved in phosphoric acid overnight at 70 ºC in individual tubes, and isotope ratios measured using either AP 2003 or VG Prism III mass spectrometers in continuous flow mode. Repeat analyses of NBS-19 and internal calcite standards are generally better than ± 0.2‰ for carbon and ± 0.3‰ for oxygen. Forty-four

hand-drilled carbonate powders were analysed for O and C isotopes at the Vrije Universiteit, Amsterdam. Carbonate samples of 50 μg weight were dissolved in individual tubes of phosphoric acid overnight at 45 ºC and analysed using a ThermoFinnigan Delta Plus with GasBench II. Repeat analyses of an internal calcite standard calibrated to NBS-19 are generally better than ±0.1‰ for carbon and ± 0.15‰ for oxygen. Oxygen isotope data would usually be corrected using fractionation factors for dolomite and calcite, such as those of Rosenbaum and Sheppard (1986). However, in this instance the samples include several calcites with near-dolomitic compositions (or calcite-dolomite mixtures, or calcitised dolostones). To aid interpretation and avoid introducing artificial trends through arbitrarily defining a Mg/Ca ratio 'cut-off' threshold for dolomite correction, we opted to present all carbonate oxygen isotope data as if the sample mineralogy were pure calcite.

Silicate $\delta^{18}O$ analysis of a 1 mg quartz sample was undertaken at SUERC by laser fluorination, with CO_2 produced measured on a VG SIRA 10 mass spectrometer (precision generally better than ± 0.2‰). XRD analysis was undertaken on nine powdered samples at St. Andrews University, with a normal detection limit of 1 to 3%. The ICDP FAR-DEEP cores remain in archive at the NGU.

Methodology: U-Pb geochronology

Targeted for chronology were 14 samples from drill core 3A; one field specimen containing dropstones from the Polisarka Sedimentary Formation; one field sample from the Ahmalahti Formation that stratigraphically overlies the Polisarka Sedimentary Formation; and three samples from the Seidorechka Volcanic Formation that stratigraphically underlies the Polisarka Sedimentary Formation. For U-Pb dating an analytical approach combining laser ablation inductively coupled plasma mass spectrometry (LA-ICP-MS) with subsequent isotope dilution thermal ionisation mass spectrometry (ID-TIMS) of grains of interest (i.e., likely younger than the existing maximum age constraint) was employed.

LA-ICPMS Screening

LA-ICPMS analyses were undertaken at the NERC Isotope Geosciences Laboratory (NIGL), UK, using a Nu Plasma HR multi-collector ICPMS. Ablation was conducted using a New Wave Research UP193SS (193nm) Nd:YAG laser system. To ensure that zircons initially analysed with the laser approach could later be recovered for ID-TIMS analyses, grains were mounted on double sided sticky tape and their exterior surfaces ablated. This is not optimal for laser ablation U-Pb and Pb-Pb data quality, but tests indicate that this approach works sufficiently well to discriminate between undesirable (detrital and xenocrystic) zircons and potentially useful volcanic zircons (< 2441 Ma, in this case).

ID-TIMS (sample 3A 20.01 m)

Zircon crystals (30–70 µm diameter) were extracted from a 29 cm long (1/4 core) sample from 20.01 m to 20.30 m depth in ICDP FAR-DEEP Hole 3A (Sample 3A 20.01 m) and analysed by ID-TIMS methods at the NIGL. The zircons were first isolated from around 300 grams of sample using conventional mineral separation techniques. Prior to undergoing ID-TIMS analyses, these zircons were subject to a modified version of the chemical abrasion technique (Mattinson, 2005). For details of sample pre-treatment, dissolution and anion exchange chemistry at NIGL see Martin et al., (2013) and references therein. Further details are given in the supplementary information.

Results

Sedimentary rock petrography

Sedimentary rocks of the Limestone member (Melezhik et al., 2013b) include finely laminated ‘limestone and siltstone couplets’ (Fig. 3). Some of the carbonate layers are continuous across the core width (Fig. 3b), while others form discontinuous lenses (see Figs. 3c and 3d; also Melezhik et

al., 2013b). The sedimentary protoliths of these layered carbonate-siliciclastic rocks were likely carbonate and quartz-rich siltstones, now metamorphosed to marbles with interlocking crystal fabrics. Some marbles are relatively pure carbonate rocks, like those found at 128.35 m (Fig. 4a), while others include layers of quartz and talc found at 182.44 m and 201.14 m (Figs. 4b and 4c).

Layered carbonate-siliciclastic rocks both below and above the peridotite body (Fig. 2) commonly contain laminae of a soft metallic grey mineral with a blue sheen in hand-specimen. In thin-section this mineral shows pleiochroism from light brown to colourless (Fig. 4d), with birefringence to 2nd order red. The mineral is therefore deduced to be talc, and this concurs with bulk rock XRD analyses (Table S1 in supplementary information). In thin-sections, several crenulated talc layers are cross-cut (replaced) by euhedral rhombs of dolomite (Fig. 4d). Talc-replacement carbonate rhombs (shown as they appear in the core in Fig. 3e) are found in abundance in other sections of the stratigraphy, particularly within the serpentinised peridotite body between 175.68 m and131.17 m (Fig. 4e). Petrographic examination reveals that komatiites at 81.69 m are also carbonatised and serpentinised (Fig. 4f).

Distinctly different in appearance to the secondary dolomite rhombs are dusty-looking and more rounded carbonate clasts conclusively identified only around 126.97 m depth (Fig. 5). These clasts are found in at least four 3 cm-thick beds separated by foliated thin carbonate layers. Staining with Alizarin Red S revealed that the clasts are dolomitic, and the sheared carbonate layers are dominantly calcitic. These rocks lack talc, but do contain laths of white mica aligned parallel layering (Fig. 5) and interpreted as the metamorphic product of clay minerals. This mica is most prominent in calcitic foliated layers (these layers lack quartz) and also occurs with small quartz crystals around the margins of dolostone clasts (but is absent in the clasts). The mineralogy deduced from petrography is consistent with bulk rock XRD analysis (Table S1; quartz, calcite, dolomite, muscovite).

Veins and veinlets comprised of quartz and carbonate, some of which are ptygmatically folded, are found in several places (Figs. 3d, 4b and 7). Their presence raises the prospect that circulating meteoric, burial or metamorphic fluids might have altered carbonate stable isotope compositions. Following acquisition of bulk rock stable isotope data (Fig. 6), carbonate rocks around a quartz vein that occupies approximately 20cm of the core at ca. 125 m depth (Figs. 2 and 7), and a 1 cm thick quartz veinlet at ca. 126.85 m, were targeted for sampling, to assess whether carbonate stable isotopic compositions were affected by vein-associated fluids. Carbonate veins were also analysed for their stable isotopic composition and include those sampled from above and below, as well as within, the peridotite body. The final phase of carbonate present is as mm-thick brown weathering alteration rims around diamictite clasts; these, too, were sampled for stable isotopic analyses using a hand-drill.

Elemental chemistry results

Elemental concentrations of powdered samples measured by XRF give data applicable to the whole rock, whereas the ICP-AES data should relate more specifically to the carbonate component. Magnesium concentrations (measured by ICP-AES) of the carbonates range from 1410 to 97600 ppm, and Mg/Ca molar ratios up to a maximum of 47% Mg (vs 53% Ca). The carbonates are therefore limestones to calcitic dolostones. Elemental analyses of bulk rock powders have not revealed any stoichiometric dolostones in these cores. On the basis of available elemental data, the main intervals of dolostone in FAR-DEEP Hole 3A are from 221 to 225 m; immediately above the peridotite at 130.94m; and from ~124 to 127.4 m. However some samples have 'out of sequence' Mg/Ca values if the trend from ~124 to 127.4 m is interpreted as purely depth- and time- related (Fig. 6). Importantly, Mg/Ca molar ratio correlates very strongly with $\delta^{13}C$ over the interval of the carbon isotope excursions (Fig. 7): the lowest $\delta^{13}C$ values are undoubtedly from Mg-rich carbonates ($n = 38$, $r = 0.85$).

Cr and Ni concentrations of acetic-acid soluble ('carbonate') components (measured by ICP-AES) also correlate very strongly with $\delta^{13}C$ between 130.82 and 124.33 m depth (see Table S2 in supplementary information). Chromium and nickel concentrations of the first carbonate sample above the peridotite are very high (38 and 12 ppm, respectively). Whole-rock Cr and Ni concentrations (measured by XRF) do not show the strong correlation with carbonate $\delta^{13}C$ between 130.82 and 124.33 m .

Strontium concentrations (ICP-AES) range from 13 to 1180 ppm. Manganese concentrations (ICP-AES) range from 8 to 3980 ppm. Mn/Sr molar ratios (ICP-AES) range from 0.33 to 23 with the highest ratio from any sample below the peridotite (Fig. 8) being 8.1. Mn/Sr (ICP-AES) molar ratios > 9 are found at 130.94 m (the first carbonate sample above the peridotite) and in all measured bulk rock samples from ~127.8 m upwards (Fig. 8). The maximum Mn/Sr ratio of 23 at 126.01 m is exceptional. Whole-rock Mn/Sr ratios (measured by XRF) are mostly lower (< 5, with a maximum measured value of 8.7). Overall Mn/Sr trends in the XRF bulk rock data are similar to those found in the ICP-AES 'carbonate' data.

Carbonate stable isotope results

Measured bulk carbonate $\delta^{13}C$ values in FAR-DEEP Hole 3A range from +0.9 to -5.4‰ (VPDB). The minimum $\delta^{13}C$ value from the 44 'hand-drilled' carbonate powders was -7.5‰, with a maximum of +0.6‰. Below 177 m depth, almost all $\delta^{13}C$ values fall in the range 0 ± 1 ‰. Above 178 m, at least two $\delta^{13}C$ excursions to minima of around -6‰ are seen (Fig. 6). The first begins at ~177.5 m, with $\delta^{13}C$ falling to -2.7‰ from a starting position 2 m below the base of the peridotite. Carbon isotopic compositions of secondary dolostone crystal growths within the peridotite were measured at -6.4‰ (sample from 135 m), while veins in the peridotite are less negative at the base

of the body (-4.0‰; 150.49 m) than at the top (-6.6‰; 132.8 m). All other secondary carbonates obtained from within the peridotitic section gave $\delta^{13}C$ compositions within this range.

The first 'bulk' carbonate sample above the peridotite (at 130.94 m) has low $\delta^{13}C$ of -5.4‰, and this was confirmed by a value of -5.8‰ from a sample of the same brown discoloured carbonate taken from 131.1 m (Fig. 6). The carbon isotope trend is towards 0‰ in the overlying carbonates, reaching 0‰ at129.78 m before declining to a nadir of -5.9‰ in dolostones at 125.60 m. There is a recovery to -1.9‰, although there is considerable scatter (Fig. 6). A final negative swing to -7.4‰ at 122.32 m is based on only one data point.

Carbonates that appear least likely to be altered on the basis of their petrography and distance from potential fluid conduits like veins gave the least negative $\delta^{13}C$ compositions, mostly near 0‰, *except* for the dolostone clasts (those of 126.97 m, shown in Fig. 5), plus one diamictite clast and one sample of 'marble' from 126.87 m. The latter comes from very close to the preserved dolostone clasts. The 'clastic' dolostone grains from 126.97 m (Fig. 5) themselves exhibit significantly more negative $\delta^{13}C$ values (-4.9 to -5.0‰) than the intervening calcite-containing sheared layers (-3.0 to -4.0‰).

All veins or likely secondary carbonates below the peridotite body gave 'normal' or 'near normal' $\delta^{13}C$ compositions, similar to the surrounding carbonate. The majority (but not quite all) veins and metamorphosed sedimentary carbonates judged to be in proximity to veins above the peridotite gave negative $\delta^{13}C$ values. In one case (129.97 m), carbonate from within a few millimetres of a vein gave $\delta^{13}C$ of -4.3‰ while carbonate 15 cm above the vein gave a value of -0.7‰. Brown-coloured (dolomitic?) alteration rims around clasts in the diamictite all gave very low $\delta^{13}C$ values, often around -7‰.

The oxygen isotope data are all isotopically light. Bulk samples gave a $\delta^{18}O$ range from -16.2 to -23.8‰ (VPDB), while 'hand drilled' sample data range from -14.7 to -25.0‰. Except for the two extreme values all other data from the hand-drilled samples lie between -16.4 and -22.3‰. It should be recalled that none of these oxygen isotope data are corrected for their Mg content.

A cross-plot of $\delta^{18}O$ vs $\delta^{13}C$ (Fig. 9) reveals some significant trends. First it is clear that the majority of all samples have $\delta^{18}O$ values between -20 and -22‰. Some of the more Mg-rich carbonates have slightly elevated $\delta^{18}O$ (Fig. 6), particularly those near the base of the hole (affecting carbonates with $\delta^{13}C$ ca. 0‰) and not correcting for Mg content (by up to -1.4‰) could partly explain this. However the population of very low $\delta^{13}C$, Mg-rich carbonates exhibits $\delta^{18}O$ compositions comparable to the majority of the 'normal' $\delta^{13}C$ carbonates, or perhaps slightly more negative than the modal value (particularly if a dolomite correction were applied). Most intriguing are a sub-set of 'calcites' (as determined by Alizarin Red S staining) with elevated $\delta^{18}O$ (up to -16.4‰) and $\delta^{13}C$ from -3.0 to -4.0‰. These seem to form a mixing line trend with 'dolomites' from the same sample (126.97m) that have low $\delta^{13}C$ and low to modal $\delta^{18}O$ compositions (Fig. 9). One sample of secondary quartz extracted from the ICDP FAR-DEEP Hole 3A cores at 223.30 m has $\delta^{18}O_{sil}$ of 11.4 ‰ (VSMOW) most likely indicating a relatively high temperature of precipitation.

U-Pb geochronology: results and interpretation

The samples targeted for chronology are summarized in Table S3 in the supplementary information, and sample depths for ICDP FAR-DEEP Hole 3A are shown on Fig. 10. Of the 19 studied samples, only eight yielded zircons. A total of 218 zircons were obtained, and all were subjected to LA-ICP-MS screening. Relative probability plots of $^{207}Pb/^{206}Pb$ ages from LA-ICP-MS for all zircon-bearing samples are shown in Fig. 10 (excluding Sample 3A 207.85 m which yielded only two Archaean dates). The maximum age of the Polisarka Sedimentary Formation (ca. 2441 Ma) is shown on each

plot (Fig. 10). Samples 3A 22.90m and Ru1310 show nine grains whose $^{207}Pb/^{206}Pb$ ages are younger than 2441 Ma. When each of the nine grains was picked and further analysed by U-Pb ID-TIMS they were shown to have Archaean ages > 2600 Ma. This discrepancy can be attributed to the larger errors associated with the LA-ICP-MS method, masking Pb-loss in the nine grains. Only zircons from an andesitic fine tuff, Sample 3A 20.01 m from ICDP FAR-DEEP Hole 3A (Fig. 11), were shown to have ages < 2441 Ma (and therefore be of potential geochronological use here) when analysed by U-Pb ID-TIMS. The results of dating of all sixteen zircon crystals obtained from Sample 3A 20.01m (Fig. S1 in supplementary information) are shown in Table 1. Of these sixteen crystals, ten yielded $^{207}Pb/^{206}Pb$ dates at ca. 2700 Ma. These grains have a prismatic nature, reflecting their xenocrystic incorporation of older material. The remaining six ID-TIMS analyses yielded $^{207}Pb/^{206}Pb$ dates from ca. 2410 to 2436 Ma (Fig. S1 and Table 1). Four of these grains (z2, z7, z8 and z9) are discordant and display correlations between $^{207}Pb/^{206}Pb$ age and magnitude of discordance (Table 1), suggesting non-zero age Pb-loss. As such, these four $^{207}Pb/^{206}Pb$ dates are likely to be inaccurate. The two remaining analyses (z11 and z12) are concordant (Fig. 12), giving overlapping $^{207}Pb/^{206}Pb$ dates of 2432.8 ± 2.1 and 2435.9 ± 1.5 Ma and an error weighted mean $^{207}Pb/^{206}Pb$ date of 2434.8 ± 1.2 Ma (assuming age equivalence of the two dated zircons and using a value of 137.88 for $^{238}U/^{235}U$ for consistency with older studies; see supplementary information). Incorporation of the uncertainties in $\lambda^{235}U$ and $\lambda^{238}U$ (Jaffey et al., 1971), required only when comparing $^{207}Pb/^{206}Pb$ dates with those from other decay schemes like Re-Os, increases the uncertainty to 6.6 Myr.

Given the potential global significance of the U-Pb date obtained, the context and petrography of the sample is described here. Rock sample 3A 20.01 m was intersected around 100 m above the top of the carbonate-bearing interval (and ca. 80 m above the diamictites), between 20.01 and 20.30 m in ICDP FAR-DEEP Hole 3A (Fig. 2). In hand specimen (Fig. 11a), altered and compacted pumice fragments (0.5 to 1 mm) have a common alignment, giving the rock a discontinuous, streaky

appearance. Lithic fragments (0.25 mm) and crystals (0.1 mm) are also present. In thin section (Fig. 11b), the altered pumice clasts (constituting 5% volume of the rock) are uniformly aligned with a eutaxitic texture, suggesting welding or in-situ diagenetic compaction. Fragments observed include volcanic quartz (3% volume) with small embayments and straight extinction, and less commonly plagioclase (1% volume). Rare lithic fragments, composed of plagioclase and pyroxene, are found in a fine groundmass of feldspar, quartz, and opaque minerals. Weak chlorite alteration is evident in the groundmass. This rock is best classified as an andesitic fine tuff (White and Houghton, 2006) on the basis of the presence of quartz and feldspar; a light to moderate colour index; the presence of pumice and fragments of crystals and (rare) lithics; and a fine groundmass. The clast type, clast morphology, and grain size range indicate that this fine tuff has not experienced interim storage prior to lithification. The morphologies of the zircon crystals (30 – 70 μm) recovered varied, with some large prismatic grains (albeit visibly metamict) with aspect ratios up to 8, and some smaller faceted grains with aspect ratios of 1.5 to 2. However there is a distinct morphological sub-population of prismatic crystals and crystal fragments with medial melt inclusion 'tunnel' traces: a feature that typifies volcanic zircon (z1, z2, z7 z8 and z11 in Fig. S1) and is characteristic of the ca. 2435 Ma population. Although post-depositional re-working is likely to have been restricted, we must also consider whether the ca. 2435 Ma zircons were inherited into the magma prior to eruption, and thus reflect a maximum age. Whilst we cannot categorically rule this out we believe it is unlikely given that (1) the dated zircons are distinctly younger than the known ca. 2441 Ma dates from underlying intrusions; (2) numerous levels were sampled for zircon (fig. 10) and whilst a number of samples did contain inherited zircons they were all >2.5 Ga; the ca. 2435 population only occurs in Sample 3A 20.01, a distinct andesitic fine tuff. Therefore, based upon the concordant U-Pb systematics, the morphology of the dated zircons, and their geological context, the $^{207}Pb/^{206}Pb$ date of 2434.8 ± 1.2/6.6 Ma (analytical/total uncertainty) is interpreted to approximate the age of the andesitic fine tuff and inferentially the age of the sampled stratigraphic level.

Discussion

U-Pb chronology and global correlations

Zircon grains from an andesitic fine tuff (Sample 3A 20.01m) yield a $^{207}Pb/^{206}Pb$ age at 2434.8 ± 1.2 Ma; this is interpreted as an eruption age, contemporaneous with sedimentation at this stratigraphic level. The age of the Polisarka Sedimentary Formation below 20.01 m in ICDP FAR-DEEP Hole 3A is therefore constrained between the inferred age of the Seidorechka Volcanic Formation at 2441 ± 1.6 Ma, and the newly derived age of Sample 3A 20.01 m at 2434.8 ± 1.2 Ma. This age range encompasses deposition of the carbonate rocks and the diamictite units in ICDP FAR-DEEP Hole 3A (Fig. 6). The SHRIMP zircon date of 2429 ± 6.6 Ma (Vrevsky et al., 2010) from units in western part of the Imandra-Varzuga Greenstone Belt that have been inferred to represent the top of the Seidorechka Volcanic Formation are broadly consistent with the ID-TIMS from the eastern sector, the slightly younger age perhaps being biased by non-zero age Pb-loss and/or analytical calibration.

These age constraints on deposition of the Polisarka Sedimentary Formation diamictite allow confident comparison with diamictite units deposited elsewhere. Palaeoproterozoic diamictite sections crop out in the Great Lakes region of North America, including the eponymous Huronian Supergroup in Canada and the Marquette Range Supergroup in the USA. Palaeoproterozoic diamictites are also known from the Transvaal Supergroup of South Africa, and the Meteorite Bore Member of Western Australia. Whilst the sedimentology of these sections is relatively well understood, the age constraints on these sections remain relatively poor.

There are three diamictite-bearing formations in the Huronian Supergroup (from oldest to youngest): Gowganda, Bruce, and Ramsay Lake. These three formations are underlain by the Thessalon Formation where zircons in the Copper Cliff rhyolite member have been dated at 2450 ±

25 Ma (ID-TIMS; Krogh et al., 1984); providing a maximum age constraint to diamictite deposition. The three diamictite-bearing formations are cross-cut by the Nipissing intrusions, dated at ca. 2200 Ma (for example 2217 ± 9 Ma; ID-TIMS on baddeleyite and rutile fractions; Corfu and Andrews, 1986). This date is therefore a minimum age constraint to diamictite deposition in the Huronian Supergroup sections. It has been noted that the diamictite-bearing Gowganda Formation is cross-cut by dykes with peperitic margins (Young et al, 2001), suggesting the youngest of the Huronian Supergroup diamictites may have been deposited at ca. 2200 Ma (if the cross-cutting dykes are equivalent to the Nipissing intrusions) or older. The Polisarka Sedimentary Formation diamictite could therefore be equivalent in age to any of the Huronian Supergroup diamictites.

The Marquette Range Supergroup, in the Menominee and Iron River – Crystal Falls Ranges area, includes the diamictite-bearing Fern Creek Formation that is in turn overlain by the Sturgeon Quartzite. The youngest detrital zircons in this latter formation yield a 2306 ± 9 Ma date (SHRIMP; Vallini et al., 2006), providing a minimum age constraint to deposition of the Fern Creek Formation diamictite. There is no robust maximum age. The temporal relationship between the Fern Creek Formation diamictite and the Polisarka Sedimentary Formation diamictite remains to be clarified.

In the Marquette Range Supergroup (Marquette Range area) the diamictite-bearing Enchantment Lake Formation has yielded detrital zircons whose youngest age is 2317 ± 6 Ma (SHRIMP; Vallini et al., 2006), providing a maximum age constraint to the formation's deposition. Furthermore, hydrothermal xenotime has been dated in the same formation at 2133 ± 11 Ma (SHRIMP; Vallini et al., 2006), giving a minimum age constraint for deposition. The Polisarka Sedimentary Formation diamictite was therefore deposited earlier than the Enchantment Lake Formation diamictite.

In South Africa the diamictite-bearing Duitschland and Boshoek Formations crop out in the Transvaal basin. The Rooihoogte Formation is commonly considered the lithostratigraphic

494 equivalent to the Duitschland Formation (Hannah et al., 2004) and contains authigenic pyrite that
495 has been dated by the Re-Os method at 2316 ± 7 Ma (Hannah et al., 2004); this is a maximum age
496 constraint to deposition of the Boshoek Formation diamictite. Rocks several units above the
497 Boshoek Formation are intruded by the Bushveld Complex, where zircons have yielded a 2054 ± 2
498 Ma date (SHRIMP; Scoates and Friedman, 2008), considered a suitable minimum age constraint to
499 the Boshoek Formation diamictite. The Polisarka Sedimentary Formation diamictite was therefore
500 deposited before the Boshoek Formation diamictite. The 2316 ± 7 Ma date for the Rooihoogte
501 Formation is also a minimum age constraint to diamictite deposition in the Duitschland Formation.
502 Several igneous units beneath the Duitschland Formation have been dated, with a zircon age at
503 2480 ± 6 Ma (SHRIMP; Nelson et al., 1999) on the Penge Formation currently providing the
504 maximum age constraint to the diamictite-bearing Duitschland Formation. Contemporaneous
505 deposition of the Duitschland and Polisarka Sedimentary formation diamictite units is permissible,
506 but far from certain, given the current age constraints on the African section.
507
508 The diamictite-bearing Meteorite Bore Member crops out in Australia's Hammersley Basin.
509 Underlying the Meteorite Bore Member by several units, zircons in a lava flow of the Woongarra
510 Rhyolite Formation have yielded a 2449 ± 3 Ma date (ID-TIMS; Barley et al., 1997). This is a
511 maximum age constraint to diamictite deposition in the Hammersley Basin. Baddeleyite grains from
512 a mafic sill that cross-cuts the Meteorite Bore Member have been dated at 2208 ± 10 Ma (SHRIMP
513 Müller et al., 2005) and are a minimum age constraint to deposition of the diamictite. The diamictite
514 deposition ages of the Meteorite Bore Member and the Polisarka Sedimentary Formation overlap,
515 which is not surprising, given that the Australian diamictite could have been deposited at any time
516 during a ca. 240 Myr interval.
517
518 The Polisarka glacial deposits could be equivalent to any of the three Huronion Supergroup
519 diamictite-bearing strata, but the loss of mass-independent fractionation of sulphur isotopes (MIF)

recorded in Canada, Africa and Fennoscandia may provide further independent constraints. The permanent disappearance of sulphur MIF occurs between the first and second diamictite in South Africa (Guo et al., 2009) and Canada (Papineau et al., 2007), suggesting that one can correlate the lower Duitschland with the Ramsay Lake, the upper Duitschland with the Bruce, and the Makganyene-Timeball Hill with the Gowganda diamictites (e.g., Melezhik et al. 2013a). If correct, then the presence in Fennoscandia of both MIF and mass-dependent fractionation in the pre-Huronian rocks (Reuschel et al., 2009), and a pronounced mass-dependent fractionation in the Huronian interval (Melezhik et al., 2013b), could reflect that the Polisarka glacial deposits correlate either with the Gowganda/Makganyene-Timeball Hill or with the upper Bruce/Duitschland diamictites. In any case the Polisarka Sedimentary Formation diamictites were certainly deposited prior to the Enchantment Lake (Marquette Range Supergroup) and Boshoek (Transvaal Supergroup) diamictite-bearing units.

We suggest here that the age of the diamictite-bearing Polisarka Sedimentary Formation is constrained to between 2434.8 ± 1.2 Ma (tuff in Polisarka Volcanic Formation) and 2441 ± 1.6 Ma (subvolvanic intrusions in Seidorchka Formation), indicating this represents an early (perhaps the earliest) Palaeoproterozoic glaciation.

Carbonate geochemistry

Sr abundances

All analysed carbonate samples from the Polisarka Sedimentary Formation carbonate rocks contain high Sr contents, ranging between 560 and 1030 ppm (767 ppm on average, n = 14). Several limestones have Sr concentrations higher than 800 ppm with a few samples containing 900–1030 ppm. Inorganic aragonites and calcites in equilibrium with modern seawater contain approximately 9000 and 1000 ppm Sr, respectively (Veizer, 1983), and Sr content in seawater has likely remained

546 near-constant through time (Steuber and Veizer, 2002). Hence the values measured from the
547 Polisarka carbonates are close to equilibrium concentrations of modern marine calcites (Veizer,
548 1983; Schlanger, 1988). However, the recrystallisation textures strongly argue for post-depositional
549 alteration of most of the analysed samples, hence for a significant Sr loss from these rocks. It has
550 been shown that each recrystallisation step in an open system reduces Sr content in the newly
551 formed calcite by a factor of 10, and in dolomite by a factor 20 (Veizer, 1983; Banner, 1995). Since
552 diagenetic and metamorphic alteration rarely takes place in an open system, the loss of Sr is
553 commonly less. Taking into account the strong petrographic evidence for recrystallisation
554 throughout the hole, the samples with 900–1000 ppm Sr are likely products of a precursor phase
555 with a very high initial Sr content, hence much of the carbonate was likely originally deposited as
556 aragonite.
557
558 *Oxygen isotopes*
559 The evidence for deformation fabrics throughout the core and likely Sr loss from the carbonates do
560 not require that every geochemical proxy has been entirely overprinted, because the requisite
561 water/rock ratios differ for each tracer (Banner, 1995). However, the invariably low (for
562 Palaeoproterozoic marine carbonates; e.g. Schidlowski et al., 1975) oxygen isotopic compositions
563 of the ICDP FAR-DEEP Hole 3A carbonates are intriguing. Veizer et al. (1992) reported carbonate
564 $\delta^{18}O$ values between -5 and -10‰ (VPDB) from the Transvaal Supergroup (South Africa) and Duck
565 Creek Dolomite (Western Australia), but from -13 to -18‰ (VPDB) in the Bruce Member
566 limestones of North America. They suggested that such low values might either reflect a non-
567 marine depositional environment for the Bruce Member, or a contribution from high latitude or
568 altitude glacial melt waters. In the case of the Polisarka Sedimentary Formation data, the
569 interpretation of these $\delta^{18}O$ values (mostly between -19 and -22‰ vs VPDB) must be left open, but
570 noting that the carbonate rocks have recrystallised in the presence of a hot fluid, such that their $\delta^{18}O$
571 values may no longer be representative of the original carbonate oxygen isotopic composition.

572 Quartz extracted from a carbonate at a depth of 223.30m with $\delta^{18}O_{sil}$ of 11.4‰ VSMOW is also
573 consistent with silica precipitation from a hot fluid (ca. 300 ^{o}C, for fluid $\delta^{18}O$ of 4‰ VSMOW;
574 Matsuhisa et al., 1979). A second overprinting of carbonate oxygen isotopic compositions by a late
575 stage meteoric or shallow burial fluid that preferentially affected calcites relative to dolomites
576 would provide an explanation for the sub-set of 'calcites' around 126 m depth with elevated $\delta^{18}O$
577 (up to -16.4‰) and $\delta^{13}C$ from -3.0 to -4.0‰. The possible oxygen isotope mixing line trend in this
578 sample (Fig. 9) would then result from mixing between 'calcite' and 'dolomite' end-members.
579
580 *Robustness of the carbonate carbon isotope signal*
581 The carbonate carbon isotopes are here of special interest because of the possibility they could
582 reflect marine dissolved inorganic carbon (DIC) prior to one of the early Palaeoproterozoic
583 glaciations, potentially aiding understanding of its cause. Interpreting the carbon isotopes in this
584 way first requires an assessment of the extent of secondary alteration and whether there might still
585 be a primary signal retrievable from the data.
586
587 The carbonates are all to varying extents recrystallised, but recrystallisation alone is not necessarily
588 an indicator that the carbon isotopes of these carbonates are reset: note that carbonates with
589 'normal' $\delta^{13}C$ are as affected by this pervasive recrystallisation as those containing the low $\delta^{13}C$
590 signal. Because interaction between carbonates and meteoric fluids commonly increases Mn
591 concentrations and decreases Sr concentrations of the rocks, marine carbonates with Mn/Sr ratios
592 <3 (e.g. Derry et al., 1992) or <10 (Kaufman and Knoll, 1995) are commonly believed to have
593 retained original seawater DIC signals in their $\delta^{13}C$. Carbonates here would all meet the Mn/Sr <10
594 criterion (mostly being between about 3 and 5) except for the first sample immediately above the
595 peridotite, and all samples from above ca. 127.8 m (Fig. 8). Using the ICP-AES Mn/Sr ratio data,
596 the $\delta^{13}C$ of all samples associated with the second and most prominent $\delta^{13}C$ excursion could be
597 considered suspect. However, these ICP-AES data are from 'bulk carbonate' so do not discriminate

between calcite of clear secondary origin and the primary dolostone clasts. The Mn/Sr values cannot be reliably used as an indicator of carbonate carbon isotope alteration in these mixed dolomite – calcite samples that contain the second prominent negative carbon isotope excursion. The XRF elemental data reflect only the whole rock (i.e. including silicate) composition. The Mn/Sr molar ratios calculated from these XRF data are all < 10, although the XRF dataset is more limited than the ICP-AES dataset here.

Correlation between carbonate oxygen isotopes and carbon isotopes can also be indicative of post-depositional alteration in cases where the oxygen isotopes have been altered. A complicating factor to using this approach here is the variable mineralogy of the carbonate samples. Correlation between carbonate $\delta^{13}C$ and $\delta^{18}O$ (Fig. 9) is best explained as the result of mixing between low $\delta^{13}C$, low $\delta^{18}O$ dolostone and high $\delta^{13}C$, high $\delta^{18}O$ secondary calcite end-members. This approach cannot therefore be used to distinguish primary from altered carbon isotope signals in this case. It is however encouraging that the dolostone clasts and secondary calcite yield different values, testifying that the carbonate carbon isotopes of ICDP FAR-DEEP Hole 3A have not been entirely overprinted by any late-stage secondary fluid interaction.

Carbon isotopes and magnesium abundances

Strong correlation between increasing Mg/Ca ratios and decreasing $\delta^{13}C$ values in some sections of ICDP FAR-DEEP Hole 3A (Fig. 6) means the origin(s) of the Mg/Ca trend may bear directly on the interpretation of the carbon isotope data. The elevated Mg in samples from 221 to 225 m is due to the presence of dolomite, although the reasons for its occurrence in this section of the core are unclear. The petrography of these sheared and recrystallised rocks is very similar to those of surrounding carbonates with more calcitic compositions. Elevated Mg/Ca values are also seen from ~124 to 127.4 m, and there are several possible explanations for this. First is the possibility that the

624 Mg derives from the adjacent ultramafic igneous rocks, perhaps during and following
625 metamorphism at greenschist grade (ca. 300ºC). This seems an attractive explanation for samples
626 taken from brown stained and chlorite-rich sections immediately above the peridotite at 130.94 m.
627 While the $\delta^{13}C$ is very low in this sample (as it is in dolomite crystals that have replaced talc in the
628 peridotite below), elemental concentrations of Ni and Cr are very high, perhaps due to alteration by
629 fluids circulating between the (Mg, Ni and Cr-rich) peridotite and overlying carbonate. However it
630 is worth noting that serpentinisation and carbonatisation of peridotite consume and do not produce
631 CO_2, although of course CO_2 flux may accompany emplacement. The isotopically negative carbon
632 isotope signatures of these carbonates (including the dolomite crystals replacing talc) must here be
633 explained either by carbon from Palaeoproterozoic sea- or meteoric water, or perhaps decarbonation
634 reactions during metamorphism, or by local alteration involving externally sourced (perhaps
635 magmatic and/or hydrothermal) fluids.
636
637 Analysis of the prominent and smoothly curved excursion to low $\delta^{13}C$ that reaches a nadir around
638 125.60 m depth shows alteration by fluids interacting with the peridotite to be untenable. This
639 second excursion occurs away from obvious bedding or structural contacts and entirely within a
640 sedimentary carbonate section (Fig. 7), separated from the peridotite body by several metres of
641 carbonate with $\delta^{13}C$ of 0 to -1‰. There are no obvious features consistent with preferential
642 channelling of diagenetic fluids through the low $\delta^{13}C$ section except some quartz veins (see Fig.
643 12). But their siliceous composition implies hot basinal fluids were silica-rich and carbon-poor, so
644 unlikely to dramatically alter $\delta^{13}C_{carb}$.
645
646 Above 130 m depth the Mg/Ca values are consistent with calcitic carbonate compositions, except
647 for between ca. 124 and 127.4 m. Here the petrography suggests the presence of (primary)
648 dolomitic clasts with some secondary calcite (Fig. 5). It seems most likely that these dolostone
649 clasts were resedimented from shallower settings. It is possible that they were derived from erosion

650 of a much older carbonate platform, although older formations in this area are not known to contain
651 any likely dolostone sources. Hence it seems reasonable to suggest that the clastic dolostone likely
652 formed in shallow waters penecontemporaneously with deeper water calcites, in the run-up to the
653 Huronian glaciation. If correct, then the carbon isotopic composition of the allochthonous dolostone
654 clasts records the pre-Huronian shallow-water marine DIC, while the deeper-water DIC is recorded
655 by the majority of the (calcitic) carbonates in ICDP FAR-DEEP Hole 3A. Correlation between
656 Mg/Ca and $\delta^{13}C$ in the carbonates between ~124 and 127.4 m (Fig. 6) could then be explained by
657 mixing lines between deep water calcites with near-zero per mil $\delta^{13}C$ and shallow-water-derived,
658 isotopically light dolostone clasts. There are clearly several plausible reasons for why the dolostone
659 clasts exhibit low $\delta^{13}C$ values. One speculative hypothesis that we cannot conclusively rule out is
660 oxidation of isotopically light methane, and its incorporation into shallow dolomite-precipitating
661 waters. Some further speculations on the possible implications of these data are given in the
662 supplementary information.
663
664 **Conclusions**
665 1. The new U-Pb data reported here constrain the onset of the Palaeoproterozoic glaciation
666 recorded by the Polisarka Diamictite to a narrow time-window between ca. 2441 ± 1.6 Ma
667 and 2434.8 ± 1.2 Ma. Considering constraints from other cratons, this glacial deposit likely
668 records one of the earliest Palaeoproterozoic glaciations, and perhaps the earliest.
669 2. The ICDP FAR-DEEP Hole 3A carbonate carbon isotope data imply Palaeoproterozoic
670 seawater DIC shallow-to-deep trends in which lighter values characterise the shallower
671 water settings. We speculate that this reflects atmospheric methane oxidation. However this
672 interpretation must be viewed with circumspection in that the carbonate carbon isotope
673 profile includes resedimented dolostone clasts that we must assume derived from
674 contemporaneous shallower settings. Further, at least some of the carbon isotope values
675 have been affected by post-depositional processes. Resolving these issues will likely require

discovery of another section containing pre-glacial carbonates of the same age, either in Fennoscandia or elsewhere in the world.

3. Geochemical data, such as the high Sr-content in the Polisarka limestones, strongly suggest aragonite precipitation from penecontemporaneous marine waters. A Polisarka "aragonite sea" might have been associated with an elevated Mg content in contemporaneous seawater.

Acknowledgements

ATB and AM were supported by NERC grant NE/G00398X/1 to AEF, ARP and DJC. VAM is supported by NFR grant 191530/V30 (projects 331000 and 802795).

References

Amelin, Y. V., Heaman, L. M., and Semenov, V. S., 1995. U-Pb geochronology of layered mafic intrusions in the eastern Baltic Shield: implications for the timing and duration of Paleoproterozoic continental rifting. Precambrian Res 75, 31-46.

Banner, J.L., 1995. Application of the Trace-Element and Isotope Geochemistry of Strontium to Studies of Carbonate Diagenesis. Sedimentology 42, 805-824.

Barley, M. E., Pickard, A. L. and Sylvester, P. J., 1997. Emplacement of a large igneous province as a possible cause of banded iron formation 2.45 billion years ago. Nature, 385: 55-58.

Bekker, A., Holland, H.D., Wang, P.-L., Rumble III, D., Stein, H.J., Hannah, J.L., Coetzee, L.L., and Beukes, N.J., 2004, Dating the rise of atmospheric oxygen: Nature, v. 427, p. 117-120.

Bots, P., Benning, L.G., Rickaby, R.E.M., S. Shaw, S., 2011. The role of SO_4 in the switch from calcite to aragonite seas. Geology, v. 39, p. 331-334.

Chashchin, V.V., Bayanova, T.B., Levkovich, N.V., 2008, Volcanoplutonic association of the early-stage evolution of the Imandra–Varzuga rift zone, Kola Peninsula, Russia: geological,

701 petrogeochemical, and isotope-geochronological data. Petrology, v. 16, p. 279–298 (in
702 Russian).
703 Corfu, F., and Andrews, A.J., 1986, A U-Pb age for mineralized Nipissing diabase,
704 Gowganda, Ontario: Canadian Journal of Earth Sciences, v. 23, p. 107–109.
705 Derry, L.A., Kaufman, A.J., Jacobsen, S.B., 1992. Sedimentary Cycling and Environmental-
706 Change in the Late Proterozoic - Evidence from Stable and Radiogenic Isotopes.
707 Geochimica et Cosmochimica Acta 56, 1317-1329.
708 Evans, D.A., Beukes, N.J., and Kirschvink, J.L., 1997, Low-latitude glaciation in the
709 Palaeoproterozoic era: Nature, v. 386, p. 262-266.
710 Evans, D.A.D., 2003, A fundamental Precambrian-Phanerozoic shift in earth's glacial style?:
711 Tectonophysics, v. 375, p. 353-385.
712 Farquhar, J., Bao, H., and Thiemens, M., 2000, Atmospheric Influence of Earth's Earliest Sulfur
713 Cycle: Science, v. 289, p. 756-758.
714 Grotzinger, J.P., and Knoll, A.H., 1995, Anomalous Carbonate Precipitates: Is the Precambrian the
715 Key to the Permian?: Palaios, v. 10, p. 578-596.
716 Guo, Q., Strauss, H., Kaufman, A.J., Schroder, S., Gutzmer, J., Wing, B., Baker, M.A., Bekker, A.,
717 Jin, Q., Kim, S.-T., and Farquhar, J., 2009, Reconstructing Earth's surface oxidation across
718 the Archaean-Proterozoic transition: Geology, v. 37, p. 399-402.
719 Halverson, G.P., Hoffman, P.F., Schrag, D.P., and Kaufman, A.J., 2002, A major perturbation of
720 the carbon cycle before the Ghaub glaciation (Neoproterozoic) in Namibia: Prelude to
721 snowball Earth?: Geochem. Geophys. Geosyst., v. 3, p. 1035.
722 Hannah, J.L., Bekker, A., Stein, H.J., Markey, R.J., Holland, H.D., 2004. Primitive Os and 2316 Ma
723 age for marine shale: implications for Paleoproterozoic glacial events and the rise of
724 atmospheric oxygen. Earth and Planetary Science Letters, v. 225, p. 43-52.
725 Haqq-Misra, J.D., Domagal-Goldman, S.D., Kasting, P.J., Kasting, J.F., 2008. A Revised, Hazy
726 Methane Greenhouse for the Archean Earth. Astrobiology 8, 1127-1137.

727 Hiess, J., Condon, D. J., McLean, N. and Noble, S. R., 2012. $^{238}U/^{235}U$ systematics in
728 terrestrial uranium-bearing minerals. Science, 335: 1610-1614.
729 Hoffman, P.F., 2013. The Great Oxidation Event and a Siderian Snowball Earth: MIF based
730 correlation of Paleoproterozoic glaciations. Chemical Geology (in press) DOI:
731 10.1016/j.chemgeo.2013.04.018
732 Hoffman, P.F., Kaufman, A.J., Halverson, G.P., and Schrag, D.P., 1998, A Neoproterozoic
733 Snowball Earth: Science, v. 281, p. 1342-1346.
734 Jaffey, A. H., Flynn, K. F., Glendenin, L. E., Bentley, W. C. and Essling, A. M., 1971.
735 Precision measurement of half-lives and specific of ^{235}U and ^{238}U. Physics Reviews, C4:
736 1889-1906.
737 Kasting, J.F., 2005, Methane and climate during the Precambrian era: Precambrian Research, v.
738 137, p. 119-129.
739 Kasting, J.F., Zahnle, K.J., and Walker, J.C.G., 1983, Photochemistry of methane in the Earth's
740 early atmosphere: Precambrian Research, v. 20, p. 121-148.
741 Kaufman, A.J., and Knoll, A.H., 1995, Neoproterozoic variations in the C-isotopic composition of
742 seawater: stratigraphic and biogeochemical implications: Precambrian Research, v. 73, p.
743 27-49.
744 Kopp, R.E., Kirschvink, J.L., Hilburn, I.A., and Nash, C.Z., 2005, The Paleoproterozoic snowball
745 Earth: A climate disaster triggered by the evolution of oxygenic photosynthesis: Proceedings
746 of the National Academy of Sciences of the United States of America, v. 102, p. 11131-
747 11136.
748 Krogh, T.E., Davis, D.W., and Corfu, F., 1984, Precise U-Pb zircon and baddeleyite ages for the
749 Sudbury area, *in* Pye, E.G., Naldrett, A.J., and Giblin, P.E., eds., The Geology and Ore
750 Deposits of the Sudbury Structure. Ontario Geological Survey Special Volume, Volume 1,
751 p. 431-446.

752 Lowenstein, T.K., Hardie, L.A., Timofeeff, M.N., and Demicco, R.V., 2003, Secular variation in
753 seawater chemistry and the origin of calcium chloride basinal brines: Geology, v. 31, p.
754 857–860.
755 Marmo, J.S., Ojakangas, R.W., 1984. Lower Proterozoic glaciogenic deposits, eastern Finland.
756 Geological Society of America Bulletin, v. 98, p. 1055-1062.
757 Martin A.P.; Condon, D.J.; Prave, A.R.; Melezhik, V.A.; Lepland, A.; Fallick, A.E.. 2013
758 Dating the termination of the Palaeoproterozoic Lomagundi-Jatuli carbon isotopic event in
759 the North Transfennoscandian Greenstone Belt. Precambrian Research, 224. 160-168.
760 10.1016/j.precamres.2012.09.010
761 Matsuhisa, Y., Goldsmith, J.R., and Clayton, R.N., 1979, Oxygen isotopic fractionation in the
762 system quartz-albite-anorthite-water: Geochimica et Cosmochimica Acta, v. 43, p. 1131-
763 1140.
764 Mattinson, J.M., 2005. Zircon U–Pb chemical abrasion (“CA-TIMS”) method: combined
765 annealing and multi-step partial dissolution analysis for improved
766 precision and accuracy of zircon ages. Chemical Geology 220, 47–66.
767 Melezhik, V.A., 2006, Multiple causes of Earth's earliest global glaciation: Terra Nova, v. 18, p.
768 130-137.
769 Melezhik, V. A., 2013, The Imandra/Varzuga Greenstone Belt. In: Melezhik, V.A., Prave, A.R.,
770 Hanski, E.J., Fallick, A.E., Lepland, A., Kump, L.R., Strauss, H. (eds.) Reading the Archive
771 of Earth’s Oxygenation. Volume 1: The Palaeoproterozoic of Fennoscandia as Context for
772 the Fennoscandian Arctic Russia - Drilling Early Earth Project. Series: Frontiers in Earth
773 Sciences. Springer, Heidelberg, p. 249-287.
774 Melezhik, V.A., Young, G.M., Eriksson, P.G., Altermann, W., Kump, L.R., Lepland, A., 2013a.
775 Huronian-age glaciations. In: Melezhik, V.A., Kump, L.R., Fallick, A.E., Strauss, H.,
776 Hanski, E.J., Prave, A.R., Lepland, A., (eds.) Reading the Archive of Earth’s Oxygenation.

777 Volume 3: Global Events and the Fennoscandian Arctic Russia - Drilling Early Earth
778 Project. Series: Frontiers in Earth Sciences. Springer, Heidelberg, p. 1059-1109.
779 Melezhik, V.A., Hanski, E.J., Prave, A.R., Lepland, A., Romashkin, A.E., Rychanchik, D.V.,
780 Brasier, A.T., Fallick, A.E., Luo, Zh-Y., Sharkov, E.V., Bogina, M.M., 2013b. Polisarka
781 Sedimentary Formation: FAR-DEEP Hole 3A. In: Melezhik, V.A., Prave, A.R., Fallick,
782 A.E., Hanski, E.J., Lepland, A., Kump, L.R., Strauss, H. (eds.), 2013. Reading the Archive
783 of Earth's Oxygenation. Volume 2: The Core Archive of the Fennoscandian Arctic Russia -
784 Drilling Early Earth Project. Series: Frontiers in Earth Sciences. Springer, Heidelberg, p.
785 530-550.
786 Mertanen, S., Halls, H. C., Vuollo, J. I., Pesonen, L. J., and Stepanov, V. S., 1999, Paleomagnetism
787 of 2.44 Ga mafic dykes in Russian Karelia, eastern Fennoscandian Shield: implications
788 for continental reconstructions. Precambrian Research, v. 98, no. 3-4, p. 197-221.
789 Müller, S. G., Krapez, B., Barley, M. E. and Fletcher, I. R., 2005. Giant iron-ore deposits of
790 the Hamersley Province related to the breakup of Paleoproterozoic Australia: new insights
791 from in situ SHRIMP dating of baddeleyite from mafic intrusions. Geology, 33: 577-580.
792 Negrutsa, V.Z., 1984. Early Proterozoic Stages of Evolution of the Eastern Baltic Shield. Nedra,
793 Leningrad, 270 pp. (in Russian).
794 Nelson, D. R., Trendall, A. F. and Altermann, W., 1999. Chronological correlations between
795 the Pilbara and Kaapvaal cratons. Precambrian Research, 97: 165-189.
796 Papineau, D., Mojzsis, S.J., Coath, C.D., Karhu, J.A., and McKeegan, K.D., 2005, Multiple sulfur
797 isotopes of sulfides from sediments in the aftermath of Paleoproterozoic glaciations:
798 Geochimica et Cosmochimica Acta, v. 69, p. 5033-5060.
799 Papineau, D., Mojzsis, S.J., and Schmitt, A.K., 2007, Multiple sulfur isotopes from
800 Paleoproterozoic Huronian interglacial sediments and the rise of atmospheric oxygen: Earth
801 and Planetary Science Letters, v. 255, p. 188-212.

802 Pavlov, A.A., Hurtgen, M.T., Kasting, J.F., and Arthur, M.A., 2003, Methane-rich Proterozoic
803 atmosphere?: Geology, v. 31, p. 87-90.
804 Pavlov, A.A., Kasting, J.F., Brown, L.L., Rages, K.A., and Freedman, R., 2000, Greenhouse
805 warming by CH_4 in the atmosphere of early Earth: J. Geophys. Res., v. 105, p. 11981-
806 11990.
807 Rosenbaum, J. M., Sheppard, S.M.F., 1986. An isotopic study of siderites, dolomites and ankerites
808 at high temperatures. Geochimica et Cosmochimica Acta, v. 50, p. 1147-1159.
809 Ravishankara, A.R., 1988, Kinetics of radical reactions in the atmospheric oxidation of CH_4:
810 Annual Review of Physical Chemistry, v. 39, p. 367-394.
811 Reuschel, M., Strauss, H., Lepland, A., Melezhik, V.A., Cartigny, P., and Kaufman, A.J., 2009,
812 Multiple sulfur isotope measurements from the 2.44 Ga Seidorechka Sedimentary
813 Formation. Geochimica et Cosmochimica Acta, v. 73, p. A1091.
814 Schidlowski M, Eichmann R, Junge CE (1975) Precambrian sedimentary carbonates: carbon and
815 oxygen isotope geochemistry and implications for the terrestrial oxygen budget.
816 Precambrian Research, v. 2, p. 1–69.
817 Schlanger, S.O., 1988. Strontium storage and release during deposition and diagenesis of
818 marine carbonates related to sea-level variations., in: Lerman, A., Meybeck, M. (Eds.),
819 Physical and Chemical Weathering in Geochemical Cycles. Kluwer, pp. 323-340.
820 Scoates, J. S. and Friedman, R. M., 2008. Precise age of the platiniferous Merensky Reef,
821 Bushveld Complex, South Africa, by the U-Pb zircon chemical abrasion ID-TIMS
822 technique. Economic Geology and the Bulletin of the Society of Economic Geologists, 103:
823 465-471.
824 Steuber, T., Veizer, A., 2002. Phanerozoic record of plate tectonic control of seawater
825 chemistry and carbonate sedimentation. Geology 30, 1123-1126.

826 Swanson-Hysell, N.L., Rose, C.V., Calmet, C.C., Halverson, G.P., Hurtgen, M.T., and Maloof,
827 A.C., 2010, Cryogenian Glaciation and the Onset of Carbon-Isotope Decoupling: Science, v.
828 328, p. 608-611.
829 Vallini, D. A., Cannon, W. F. and Schulz, K. J., 2006. Age constraints for Paleoproterozoic
830 glaciation in the Lake Superior region: detrital zircon and hydrothermal xenotime ages for
831 the Chocolay Group, Marquette Range Supergroup. Canadian Journal of Earth Sciences, 43:
832 571-591.
833 Veizer, J., 1983. Trace elements and isotopes in sedimentary carbonates. Reviews in
834 Mineralogy 11, 265-299.
835 Veizer, J., Clayton, R. N., and Hinton, R. W., 1992, Geochemistry of Precambrian carbonates: IV.
836 Early Paleoproterozoic (2.25 ± 0.25 ga) seawater: Geochimica et Cosmochimica Acta, v.
837 56, no. 3, p. 875-885.
838 Vrevsky, A.B., Bogomolov, E.S., Zinger, T.F., and Sergeev, S.A., 2010, Polychronic sources and
839 isotopic age of the volcanogenic complex (Arvarench unit) of the Imandra-Varzuga
840 structure, Kola Peninsula. Doklady (Transactions) of the Russian Academy of Sciences, v.
841 431, p. 386–389.
842 White, J.D.L., Houghton, B.F., 2006. Primary volcaniclastic rocks. Geology 34,
843 677–680.
844 Young, G. M., 1991, The geological record of glaciation: relevance to the climatic history of the
845 Earth: Geoscience Canada, v. 18, p. 100-108.
846 Young, G.M., Long, D.G.F., Fedo, C.M., and Nesbitt, H.W., 2001, Paleoproterozoic Huronian
847 basin: product of a Wilson cycle punctuated by glaciations and a meteorite impact:
848 Sedimentary Geology, v. 141-142, p. 233-254.
849
850
851

852 Figures and captions

853

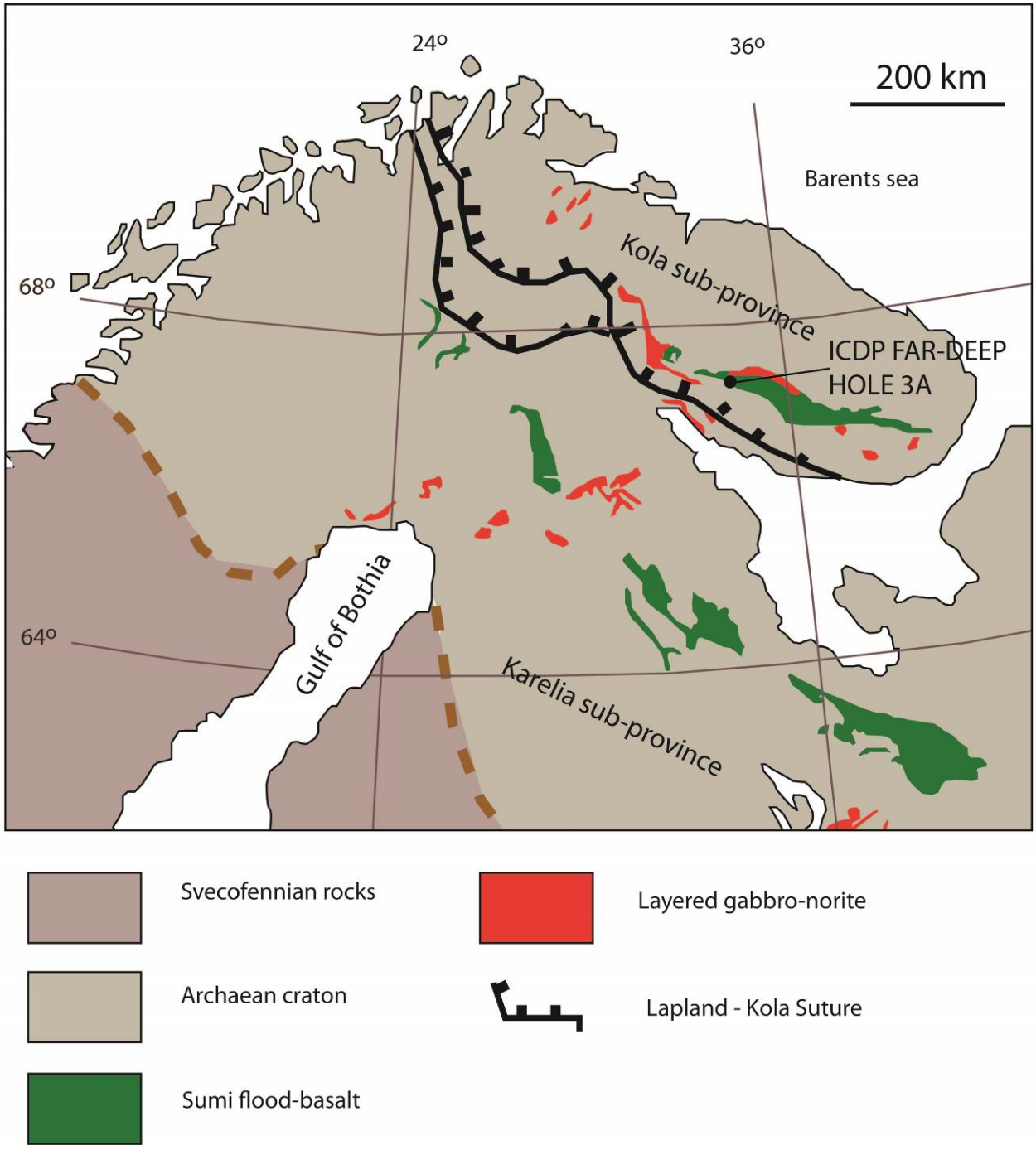

854

855 **Fig. 1** Map showing the location of ICDP FAR-DEEP Hole 3A in Fennoscandian Russia

856

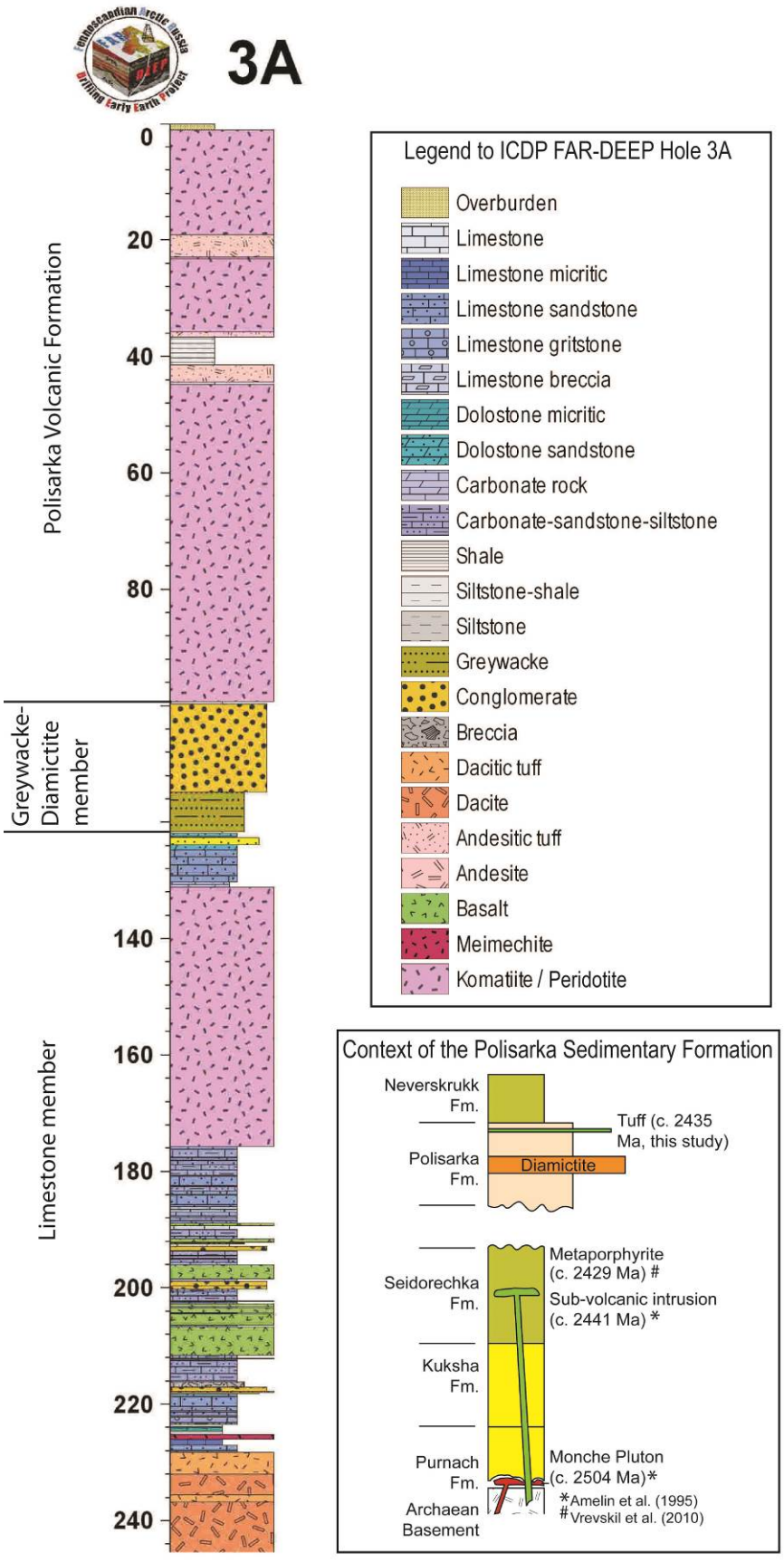

857

858 **Fig. 2** Stratigraphy (based on ICDP FAR-DEEP Database) and stratigraphic context of ICDP FAR-

859 DEEP Hole 3A

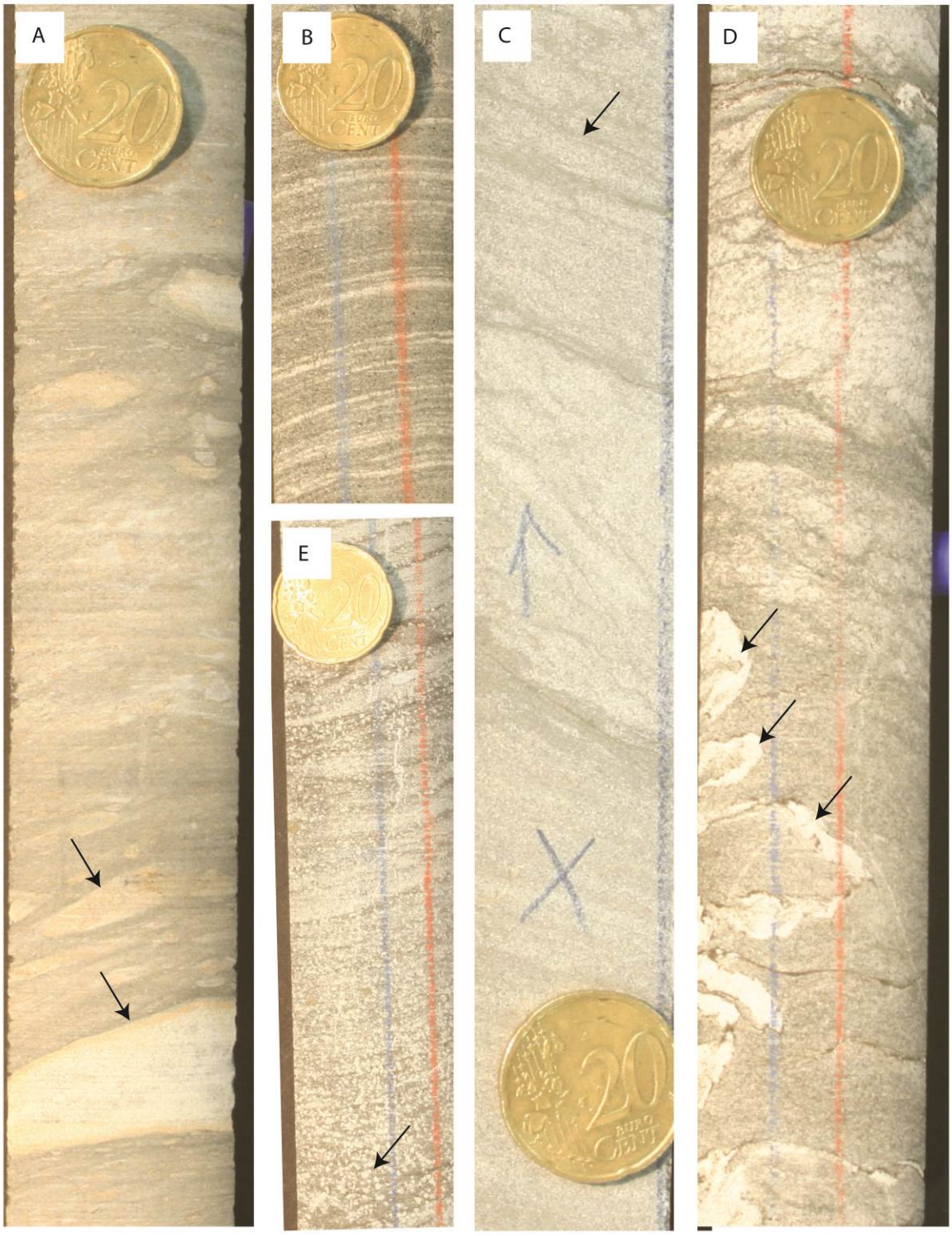

Fig. 3 Images of Polisarka Sedimentary Formation rocks, mostly from cores of ICDP FAR-DEEP Hole 3A. A) Sheared and flattened lonestones (some denoted by arrows) in a diamictite at 114.36m. Note the yellow-discoloured dolomitic alteration rims of some of these clasts: these gave low $\delta^{13}C$ values. B) Layered siltstone-carbonate couplets of possible 'varve-like' origin (178.93m depth). C)

Deformed layered siltstone-carbonate rocks showing discontinuous lenses of carbonate (one example arrowed; 190.52m). D) Sheared and folded carbonate-siliciclastic rock, including a ptygmatically folded quartz vein (arrowed; 180.25m. E) Talc-rich rock containing numerous dolostone crystals of secondary origin (dolostone crystals are white spots, one of which is arrowed; 212.19m). F) Dropstone from an outcrop of the Polisarka Sedimentary Formation. G) Andesitic dropstones in diamictite (ICDP FAR-DEEP Hole 3A, 101.4 m depth; core width is 5 cm). Coin for scale (A-E) is 20mm diameter. Photographs 3F and 3G reproduced with kind permission of Springer Science+Business Media from Victor A. Melezhik, Grant M. Young, Patrick G. Eriksson, Wladyslaw Altermann, Lee R. Kump, and Aivo Lepland (2013) 7.2 Huronian-Age Glaciation. In: V.A. Melezhik, L.R. Kump, A.E. Fallick, H. Strauss, E.J. Hanski, A.R. Prave, A. Lepland (eds.), Reading the Archive of Earth's Oxygenation, Volume 3: Global Events and the Fennoscandian Arctic Russia - Drilling Early Earth Project, pp. 1059-1109. Copyright Springer Science+Business Media 2013.

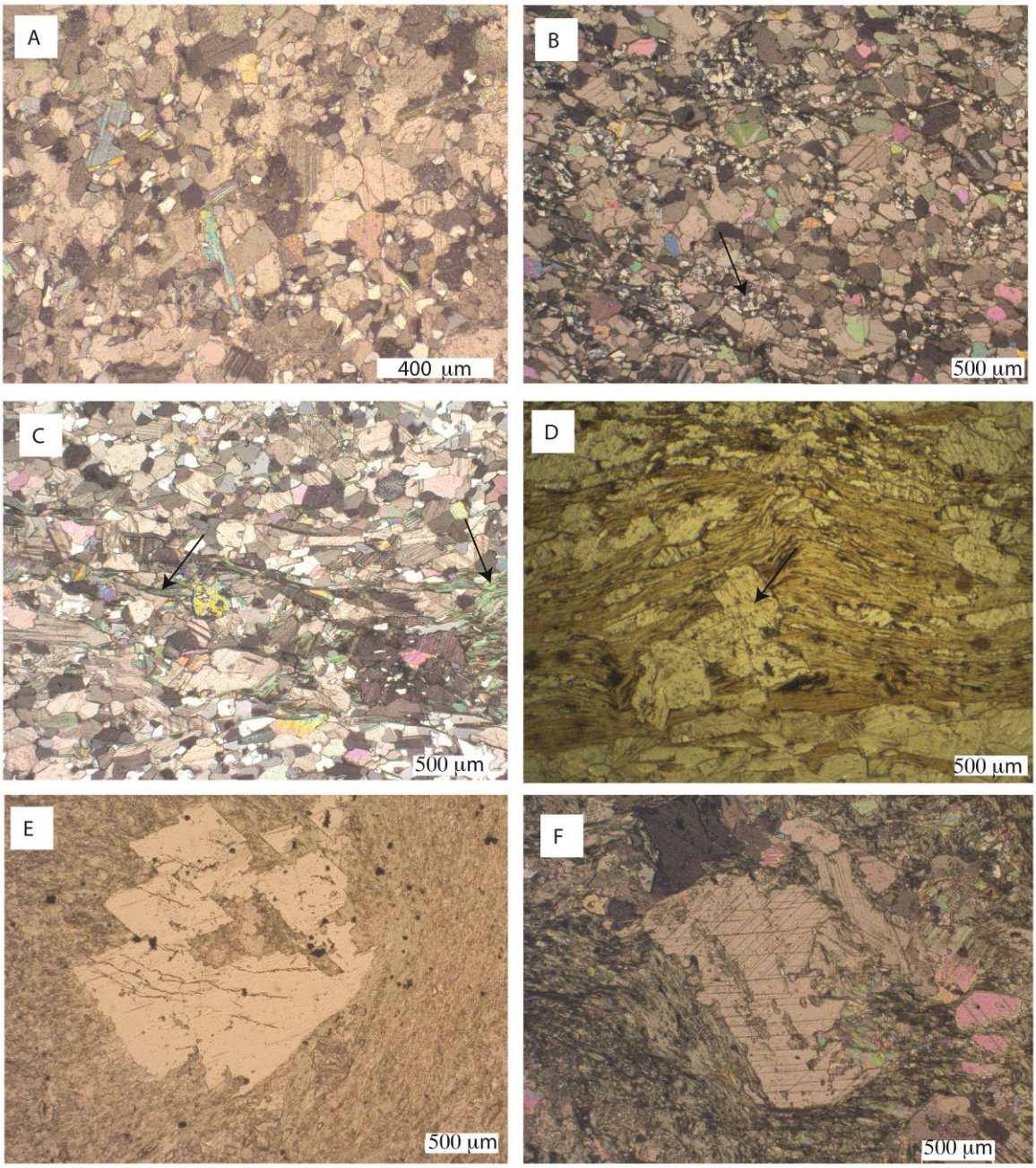

Fig. 4. Thin-sections of carbonate rocks in ICDP FAR-DEEP Hole 3A. A) Relatively homogenous carbonate rock from 128.35m as seen in cross-polarised light. B) Carbonate rock from 182.44m, in cross-polarised light. Note the quartz patches between some of the carbonate crystals (arrowed). C) Carbonate rock with layers of talc (arrowed) from 201.14m in cross-polarised light. D) A layer of talc (brown crenulated mineral) with a dolomite rhomb (arrowed) that has overgrown the talc (212.19m). E) A dolomite rhomb that has overgrown talc within the peridotite body (147.23m). F) A carbonate rhomb from a carbonatised komatiite at 81.69m.

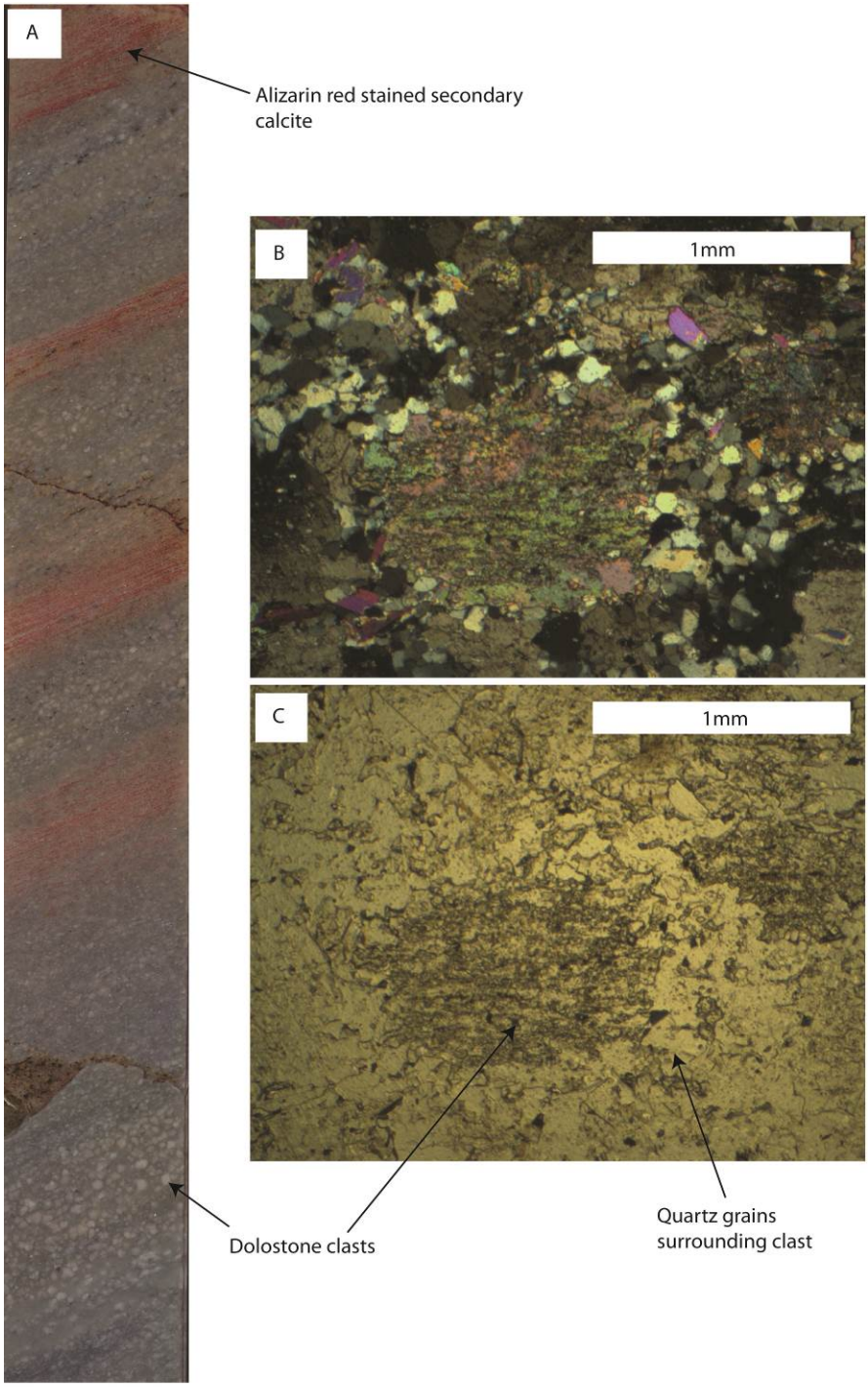

Fig. 5 The clastic dolostone found at 126.97 m depth in ICDP FAR-DEEP Hole 3A. A) Hand-specimen, stained with Alizarin Red S to distinguish calcite (red-stained layers) from dolomite (clasts left unstained). B) Thin-section showing a dolomitic clast under cross-polarised light. Note that quartz grains surround the dolostone clast in the centre. C) Same dolomitic clast viewed in plane polarised light.

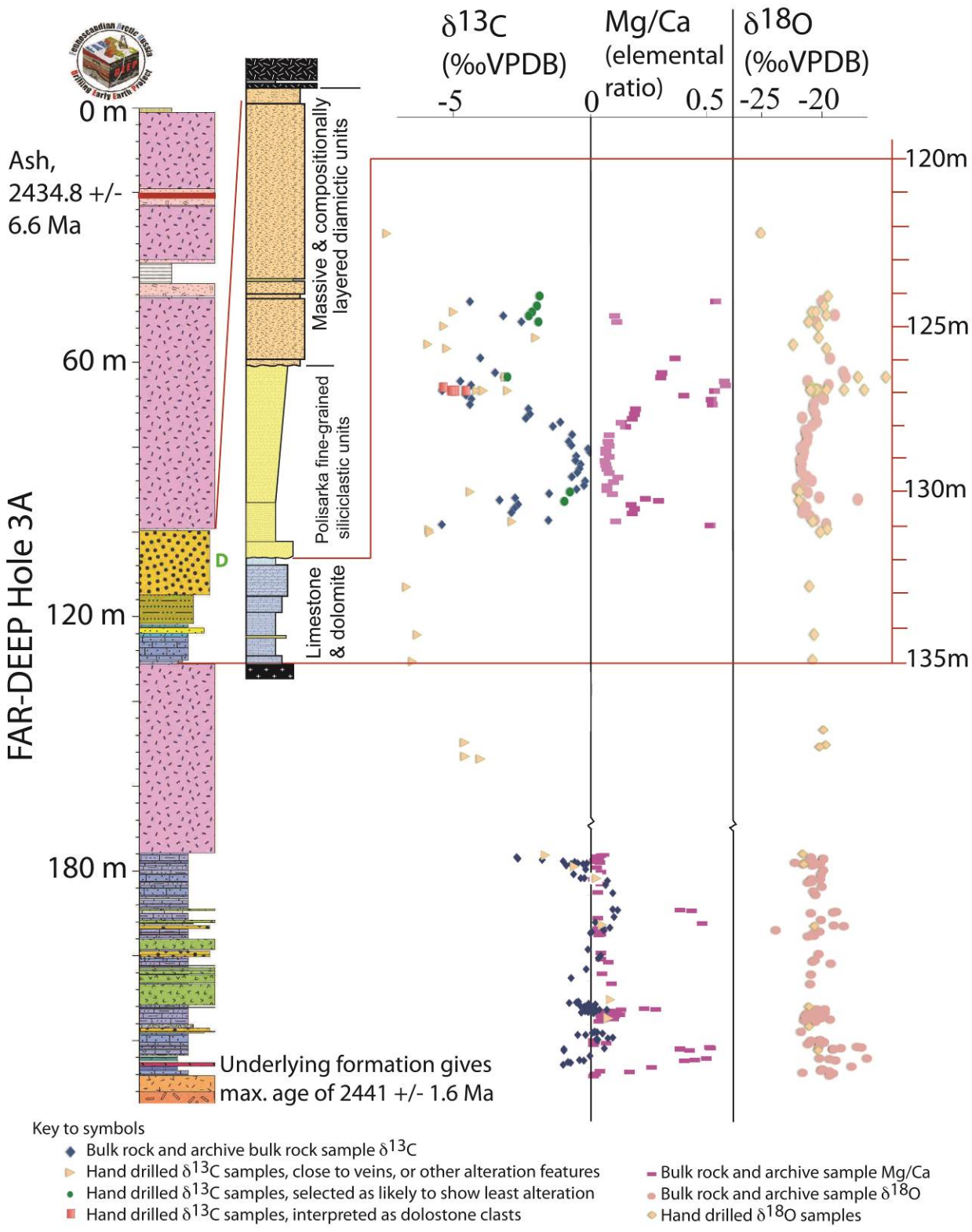

Fig. 6. Carbonate rock geochemistry, including carbon isotopes, oxygen isotopes, and Mg/Ca ratios. For symbols see the legend and Fig. 2. Note that the data inside the red box all belong to the carbonate unit between the peridotite and diamictite. Two excursions to low $\delta^{13}C$ values are seen as the base of the diamictite is approached. Secondary carbonate within the peridotite body also gives low $\delta^{13}C$ values. The second excursion at 126.97m is linked to resedimented

dolostone clasts. Secondary calcite layers in that same area give higher $\delta^{13}C$ values. Mg/Ca ratios correlate strongly with $\delta^{13}C$ in the area of the excursions. Oxygen isotope values are invariably low, and trends seem to reflect carbonate Mg content.

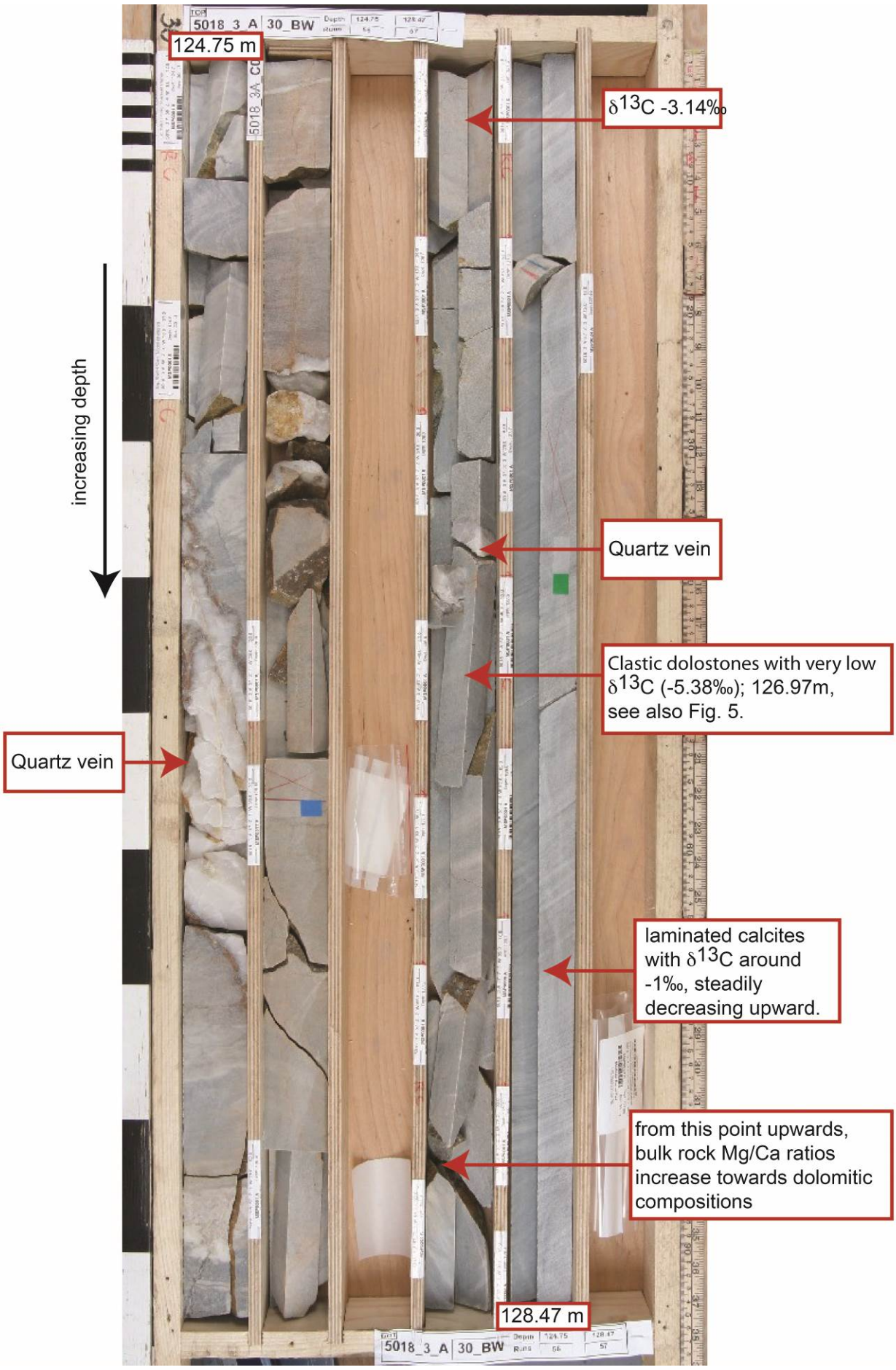
124.75 m
δ13C -3.14‰
increasing depth
Quartz vein
Clastic dolostones with very low δ13C (-5.38‰); 126.97m, see also Fig. 5.
Quartz vein
laminated calcites with δ13C around -1‰, steadily decreasing upward.
from this point upwards, bulk rock Mg/Ca ratios increase towards dolomitic compositions
128.47 m

905

Fig. 7 Photograph of the rocks between 128.47 m and 124.75 m depth in ICDP FAR-DEEP Hole 3A. Note that this section starts with laminated calcites, and includes low $\delta^{13}C$ allochthonous dolostone clasts. Note also the quartz veins, around which the carbonates also have low $\delta^{13}C$ values.

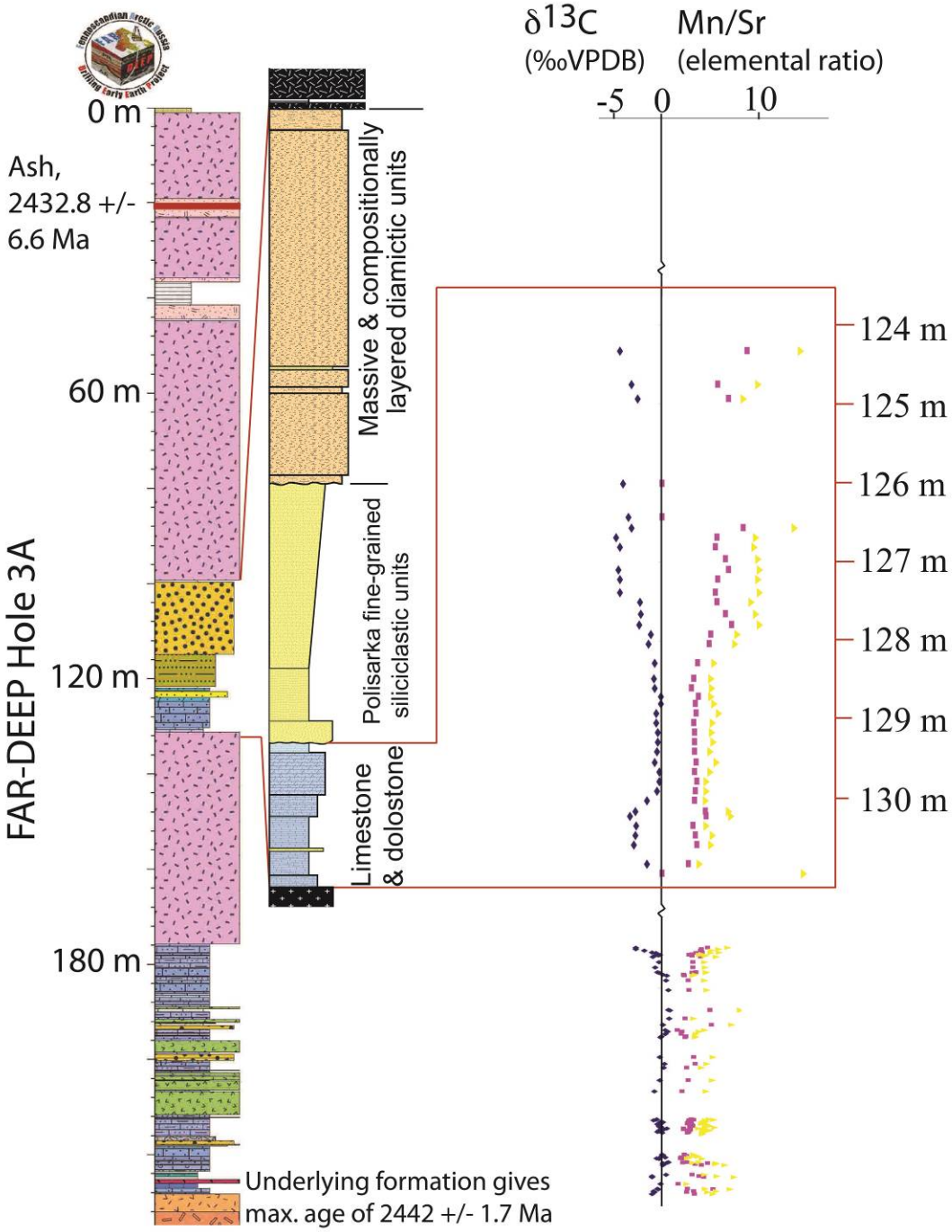

Fig. 8 Carbonate $\delta^{13}C$ (bulk rock samples) and Mn/Sr ratios (for the same bulk-rock samples). For stratigraphic symbols see Fig. 2. Mn/Sr ratios shown in yellow were determined by ICP-

AES whereas those in pink were determined by XRF. Note that the data within the red box belong to the carbonate unit between the peridotite and diamictite.

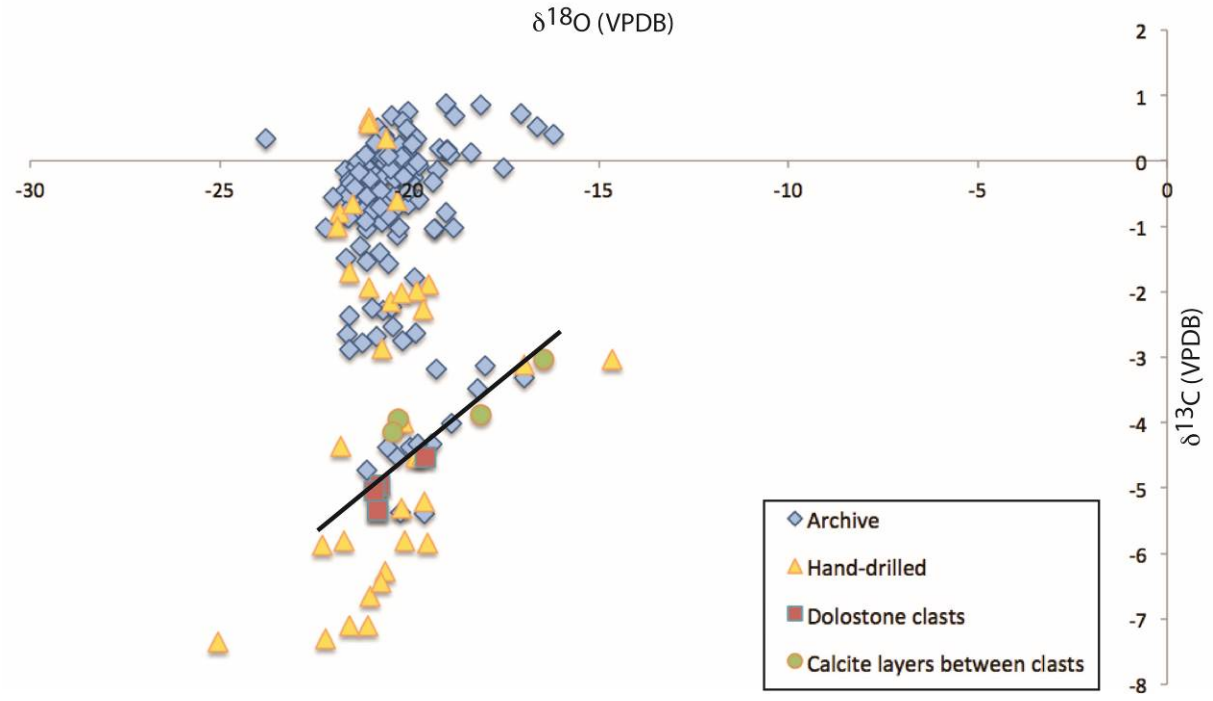

Fig. 9 A cross-plot of carbonate $\delta^{18}O$ (x-axis) vs $\delta^{13}C$ (y-axis). For symbols see the legend. Oxygen isotope values are not corrected for their Mg content (data presented as if samples were all calcite). Their oxygen isotope values are relatively invariant, hence the trend mostly runs parallel to the Y axis. A possible mixing-line trend (black line) likely reflects mixing between 'calcite' and 'dolomite' end-members. See text for discussion.

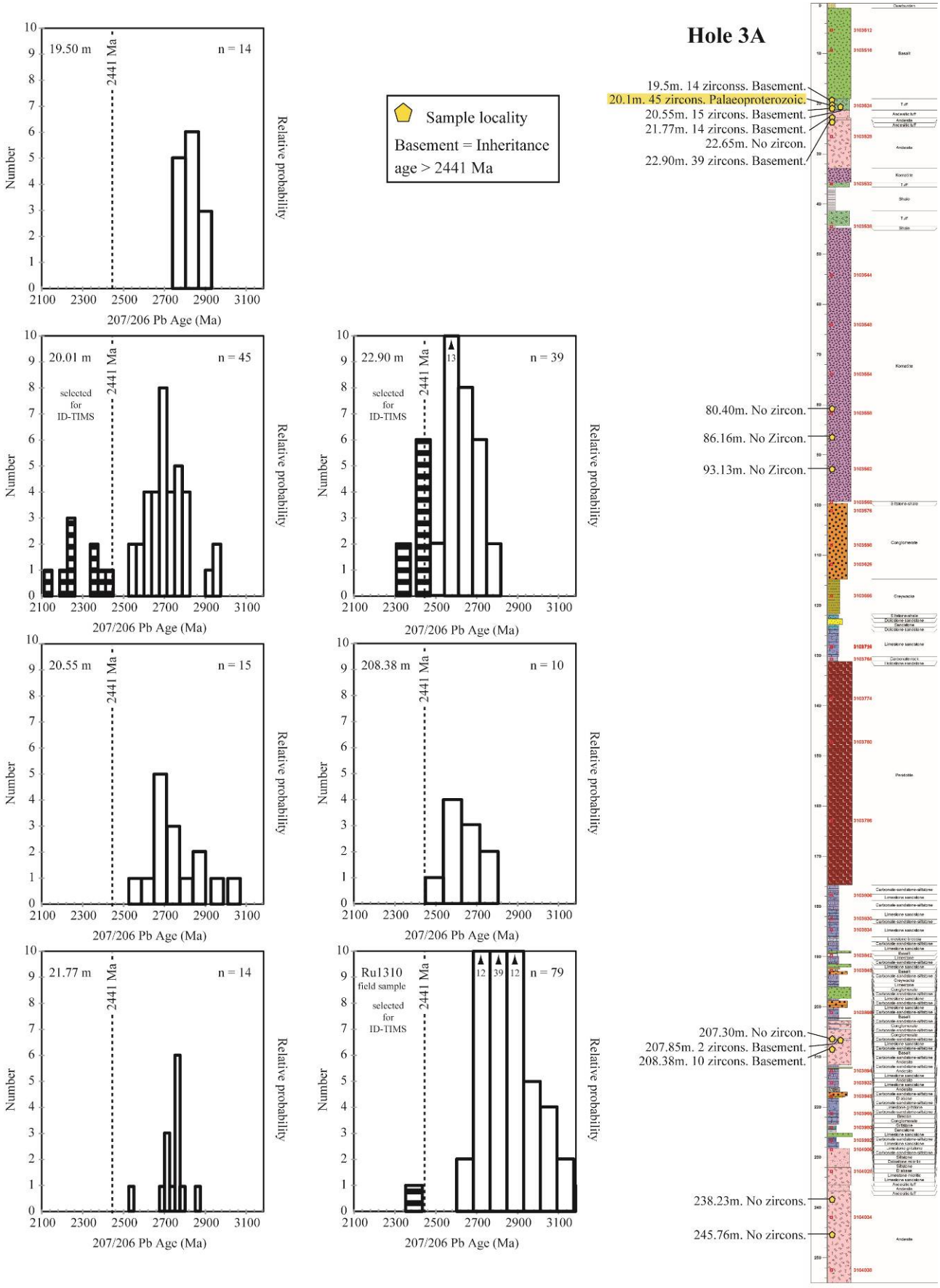
Hole 3A
19.5m. 14 zirconss. Basement.
20.1m. 45 zircons. Palaeoproterozoic.
20.55m. 15 zircons. Basement.
21.77m. 14 zircons. Basement.
22.65m. No zircon.
22.90m. 39 zircons. Basement.
80.40m. No zircon.
86.16m. No Zircon.
93.13m. No Zircon.
207.30m. No zircon.
207.85m. 2 zircons. Basement.
208.38m. 10 zircons. Basement.
238.23m. No zircons.
245.76m. No zircons.
Sample locality
Basement = Inheritance
age > 2441 Ma
19.50 m
n = 14
20.01 m
n = 45
selected for ID-TIMS
20.55 m
n = 15
21.77 m
n = 14
22.90 m
n = 39
208.38 m
n = 10
Ru1310
field sample
selected for ID-TIMS
n = 79
2441 Ma
Number
Relative probability
207/206 Pb Age (Ma)

923

924 **Fig. 10** $^{207}Pb/^{206}Pb$ histogram plots of LA-ICPMS data for samples targeted for chronology and the
925 location of samples from drill core 3A. Sample Ru1310 was collected in the field at 67° 11.984 N and 35° 46.361 E. Lithological column is based on FAR-DEEP Database.

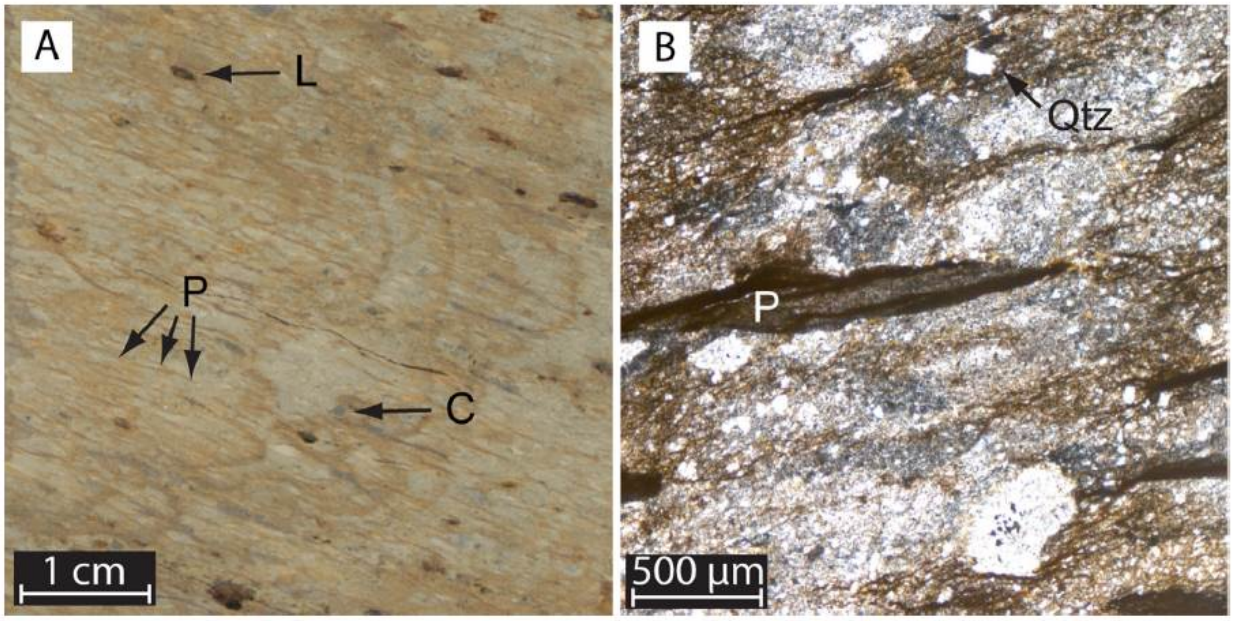

927

928 **Fig. 11** Petrography of drill core sample 3A 20.01 m (ash from which zircons were obtained). A)
929 Hand specimen. L = lithic. P = pumice. C = crystal. B) Thin section. P = pumice. Qtz =
930 quartz (volcanic).

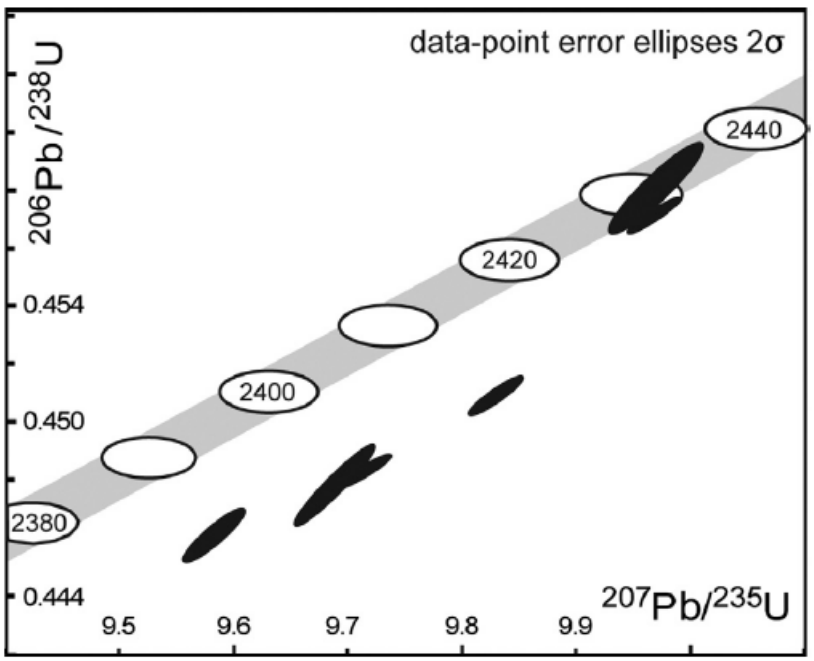

931

932 **Fig. 12:** Conventional concordia plot for zircons analysed from sample 3A 20.01 m.

Fraction	Th/U	$^{206}Pb^*$ x10^{-13} mol	mol % $^{206}Pb^*$	Pb^*/Pb_c	Pb_c (pg)	$^{206}Pb/^{204}Pb$	$^{208}Pb/^{206}Pb$	$^{207}Pb/^{206}Pb$	% err	$^{207}Pb/^{235}U$	% err	$^{206}Pb/^{238}U$	% err	corr. coef.	$^{207}Pb/^{206}Pb$	±	$^{207}Pb/^{235}U$	±	$^{206}Pb/^{238}U$	±
(a)	(b)	(c)	(c)	(c)	(c)	(d)	(e)	(e)	(f)	(e)	(f)	(e)	(f)		(g)	(f)	(g)	(f)	(g)	(f)
z2	0.787	4.1196	99.61%	86	1.37	4397	0.224	0.156904	0.089	9.688111	0.293	0.447821	0.254	0.957	**2422.5**	1.5	2405.6	2.7	2385.6	5.1
z3	0.486	12.0116	99.88%	280	1.17	15203	0.135	0.189230	0.080	13.728777	0.173	0.526188	0.103	0.959	2735.4	1.3	2731.2	1.6	2725.4	2.3
z4	0.472	1.6033	99.33%	49	0.90	2718	0.131	0.189681	0.096	13.794564	0.337	0.527453	0.303	0.961	2739.3	1.6	2735.7	3.2	2730.8	6.7
z6	0.331	1.4206	98.87%	27	1.39	1499	0.101	0.198730	0.222	12.805982	0.440	0.467355	0.374	0.864	2815.7	3.6	2665.5	4.1	2472.0	7.7
z7	1.040	7.5733	99.54%	72	3.15	3346	0.296	0.157161	0.090	9.714832	0.177	0.448323	0.098	0.949	**2425.3**	1.5	2408.1	1.6	2387.8	2.0
z8	0.968	3.8219	98.99%	32	3.49	1523	0.275	0.155794	0.099	9.582447	0.224	0.446091	0.158	0.922	**2410.5**	1.7	2395.5	2.1	2377.9	3.1
z9	0.938	6.6041	99.42%	57	3.44	2664	0.266	0.158101	0.093	9.829474	0.191	0.450913	0.117	0.927	**2435.4**	1.6	2418.9	1.8	2399.4	2.3
z11	0.939	1.2339	98.17%	18	2.02	882	0.264	0.157854	0.123	9.969447	0.332	0.458051	0.275	0.935	**2432.8**	2.1	2432.0	3.1	2431.0	5.6
z12	0.461	7.0665	99.46%	54	3.47	2820	0.130	0.158146	0.089	9.967708	0.182	0.457125	0.105	0.946	**2435.9**	1.5	2431.8	1.7	2426.9	2.1
z13	0.512	9.3420	99.77%	140	1.84	7239	0.141	0.198694	0.085	15.005791	0.186	0.547739	0.120	0.935	2815.5	1.4	2815.6	1.8	2815.8	2.7
z31	0.354	1.7701	94.52%	5	9.42	268	0.100	0.194517	0.216	13.892947	0.736	0.518008	0.689	0.956	2780.7	3.5	2742.4	7.0	2690.8	15.2
z39	0.251	0.2721	91.03%	3	2.37	177	0.073	0.169418	0.858	10.483936	1.854	0.448811	1.567	0.887	2551.8	14.4	2478.5	17.2	2390.0	31.3
z43	0.146	1.2562	99.38%	49	0.65	2955	0.040	0.188104	0.096	13.695541	0.352	0.528057	0.318	0.964	2725.6	1.6	2728.9	3.3	2733.3	7.1
z44	0.581	0.5824	98.17%	18	0.90	994	0.159	0.194837	0.153	14.615500	0.689	0.544053	0.667	0.975	2783.4	2.5	2790.5	6.6	2800.5	15.1
z15	0.510	0.5825	93.76%	5	3.49	246	0.139	0.189949	0.230	14.193600	0.734	0.541943	0.691	0.949	2741.7	3.8	2762.7	7.0	2791.6	15.7
z23	0.730	2.3370	98.69%	24	2.75	1196	0.202	0.185026	0.102	13.224841	0.529	0.518391	0.504	0.981	2698.4	1.7	2695.8	5.0	2692.4	11.1

(a) z1, z2 etc. are labels for fractions composed of single zircon grains or fragments; all fractions annealed and chemically abraded after *Mattinson* [2005].
(b) Model Th/U ratio calculated from radiogenic 208Pb/206Pb ratio and 207Pb/235U age.
(c) Pb* and Pbc represent radiogenic and common Pb, respectively; mol % $^{206}Pb^*$ with respect to radiogenic, blank and initial common Pb.
(d) Measured ratio corrected for spike and fractionation only.
(e) Corrected for fractionation, spike, and common Pb; up to 1 pg of common Pb was assumed to be procedural blank: 206Pb/204Pb = 18.20 ± 0.50%; 207Pb/204Pb = 15.65 ± 0.40%; 208Pb/204Pb = 38.20 ± 0.75% (all uncertainties 1-sigma). Excess over blank was assigned to initial common Pb.
(f) Errors are 2-sigma, propagated using the algorithms of *Schmitz and Schoene* [2007] and *Crowley et al.* [2007].
(g) Calculations are based on the decay constants of *Jaffey et al.* [1971]. 206Pb/238U and 207Pb/206Pb ages corrected for initial disequilibrium in 230Th/238U using Th/U [magma] = 4. 206Pb/238U dates in bold are those used in the weighted mean zircon date calculation

Table 1: U-Th-Pb data for zircons analysed from sample ICDP FAR-DEEP Hole 3A 20.01

m**Supplementary information**

U-Pb geochronology methods

For U-Pb ID-TIMS analyses the EARTHTIME ^{205}Pb-^{233}U-^{235}U (ET535) tracer solution was used, and measurements were performed on a Thermo Triton TIMS machine. Lead analyses were measured in dynamic mode on a MassCom secondary electron multiplier (SEM) detector and

corrected for 0.14 ± 0.04%/u. mass fractionation. Linearity and dead-time corrections on the SEM were monitored through repeated analyses of NBS 982, NBS 981 and U500. Uranium was measured in dynamic mode on the SEM detector. Uranium was run as the oxide and corrected for isobaric interferences with an $^{18}O/^{16}O$ composition of 0.00205 (IUPAC value and determined through direct measurement at NIGL). Uranium-lead dates and uncertainties were calculated using the algorithms of Schmitz and Schoene (2007) and a $^{235}U/^{205}Pb$ ratio for ET535 of 100.18. All common Pb in the analyses was attributed to the blank, and subsequently subtracted from sample data based on the isotopic composition and associated uncertainties analysed over time. Recent studies (Hiess et al., 2012) suggest that the natural $^{238}U/^{235}U$ ratio should not be considered invariant and a value of 137.818 ± 0.045 should be used in place of the value of 137.88 most commonly applied. Using this Hiess et al. (2012) value will lower $^{207}Pb/^{206}Pb$ dates by 0.8 ± 0.6 Myr. However, for easy comparison with the existing literature, a $^{238}U/^{235}U$ ratio = 138.88 has been employed in this study. In Table S4 (supplementary material) we quantify the affect the $^{238}U/^{235}U$ ratio has on $^{207}Pb/^{206}Pb$ geochronology by calculating both $^{238}U/^{235}U$ = 137.88 and 137.818 ± 0.045 for the samples of interest to this study.

Captions for supplementary figure and tables

Figure S1. Transmitted light photograph of zircons fro sample 3A 20.01 m analysed by CA-ID-TIMS. Each zircon is identified by a number (z1, z2, etc.) which is keyed to the data in Table X. Dates displayed next to each zircon are $^{207}Pb/^{206}Pb$ dates. Note the medial melt inclusions 'tunnel' trace that can be seen in z1, z2, z7 z8 and z11, a morphologic feature that typifies volcanic zircon.

Depth (MCD)	**126.97**	**127.22**	**128.7**	**130.58**	**130.94**	**176.5**	**178.44**	**192.6**	**195.06**
Quartz (%)	21	29	3	23	28	20	9	11	27
Calcite (%)	3	1	79	35	1	41	43	7	55
Dolomite (%)	71	63	8	24	41			75	3
Chlorite (%)		1	7	10	20				15
Muscovite (%)	5	6							
Talc (%)			3		7	16	20		
Plagioclase (%)				8	3	11	6		
Biotite (%)						12	13	7	
Sepiolite (%)							9		
$\delta^{13}C_{carb}$ (VPDB)	-5.38	-4.33	-0.15	-2.89	-5.39	-2.68	-0.94	0.09	-0.05

Table S1: XRD data for selected bulk rock ICDP FAR-DEEP Hole 3A samples

Element(s)	Correlation with $\delta^{13}C$ (r, n=38)
TiO_2	0.85
Ti (AES)	0.05
Mg/Ca	0.85
Al_2O_3	0.81
Al (AES)	0.14
Fe_2O_3 (XRF)	0.88
Fe (AES)	0.91 (exc. 130.94, v high Fe)
SiO_2	0.15
Mn (AES)	0.24
K_2O	0.53
Cr (XRF)	0.58 (exc. 130.94. which has v high Cr)
Cr (AES)	0.93 (exc. 130.94, v v high Cr)
Ni (XRF)	0.45 (exc. 130.94)
Ni (AES)	0.87
$\delta^{18}O$	0.41

Table S2: R values (n=38) of $\delta^{13}C$ vs elements for the section containing the negative carbon isotope excursions

#	Sample ID	Lithology	Formation	Sample Type	Sample weight	Zircons recovered	No. of grains	Range of ^{207}Pb / ^{206}Pb ages (Ma)
1	3A 19.50 m	Tuff (felsic)	Polisarka Sed.	core	< 500 g	yes	14	2700 - 2900
2	3A 20.01 m	Tuff (felsic)	Polisarka Sed.	core	< 500 g	yes	45	2100 - 3000
3	3A 20.55 m	Tuff (felsic)	Polisarka Sed.	core	< 500 g	yes	15	2500 - 3000
4	3A 21.77 m	Sedimentary	Polisarka Sed.	core	< 500 g	yes	14	2500 - 2900
5	3A 22.65 m	Sedimentary	Polisarka Sed.	core	< 500 g	no	0	-
6	3A 22.90 m	Sedimentary	Polisarka Sed.	core	< 500 g	yes	39	2300 - 2800
7	3A 80.40 m	Igneous (mafic)	Polisarka Sed.	core	< 500 g	no	0	-
8	3A 86.16 m	Igneous (mafic)	Polisarka Sed.	core	< 500 g	no	0	-
9	3A 93.13 m	Igneous (mafic)	Polisarka Sed.	core	< 500 g	no	0	-
10	3A 207.30 m	Igneous (intermediate)	Polisarka Sed.	core	< 500 g	no	0	-
11	3A 207.85 m	Igneous (intermediate)	Polisarka Sed.	core	< 500 g	yes	2	2800
12	3A 208.38 m	Igneous (intermediate)	Polisarka Sed.	core	< 500 g	yes	10	2450 - 2800
13	3A 238.23 m	Igneous (intermediate)	Polisarka Sed.	core	< 500 g	no	0	
14	3A 245.76 m	Igneous (intermediate)	Polisarka Sed.	core	< 500 g	no	0	
15	Ru1310	Sedimentary (dropstones)	Polisarka Sed.	Field	> 20 kg	yes	79	2600 - 3200
16	Ru6710	Igneous (mafic)	Ahmalahti	Field	> 5 kg	no	0	-
17	Ru0711	Igneous (intermediate)	Seidorechka Vol.	Field	> 5 kg	no	0	-
18	Ru2510	Igneous (intermediate)	Seidorechka Vol.	Field	> 5 kg	no	0	-
19	Ru2610	Igneous (intermediate)	Seidorechka Vol.	Field	> 5 kg	no	0	-

Table S3: Summary of the samples targeted for chronology

Table S4 Summary of interpreted $^{207}Pb/^{206}Pb$ dates and uncertainties related to choice of $^{238}U/^{235}U$ ratio.

Sample	Reference	Rock Type	Analysis	Isotopic ratios	Calculated Dates	
				^{207}Pb -	^{207}Pb -	^{207}Pb -

				^{206}Pb	±	^{206}Pb (a)	± (b)	^{206}Pb (c)	± (d)
3A 20.01m	This study	Tuff	z2	0.1569	0.09	2422.5	1.5	2422.6	1.71
3A 20.01m	This study	Tuff	z3	0.1892	0.08	2735.4	1.3	2735.5	1.54
3A 20.01m	This study	Tuff	z4	0.1897	0.10	2739.3	1.6	2739.4	1.77
3A 20.01m	This study	Tuff	z6	0.1987	0.22	2815.7	3.6	2815.8	3.72
3A 20.01m	This study	Tuff	z7	0.1572	0.09	2425.3	1.5	2425.3	1.72
3A 20.01m	This study	Tuff	z8	0.1558	0.10	2410.5	1.7	2410.5	1.86
3A 20.01m	This study	Tuff	z9	0.1581	0.09	2435.4	1.6	2435.5	1.77
3A 20.01m	This study	Tuff	z11	0.1579	0.12	2432.8	2.1	2432.8	2.23
3A 20.01m	This study	Tuff	z12	0.1581	0.09	2435.9	1.5	2435.9	1.71
3A 20.01m	This study	Tuff	z13	0.1987	0.09	2815.5	1.4	2815.5	1.61
3A 20.01m	This study	Tuff	z31	0.1945	0.22	2780.7	3.5	2780.7	3.63
3A 20.01m	This study	Tuff	z39	0.1694	0.86	2551.8	14.4	2551.9	14.39
3A 20.01m	This study	Tuff	z43	0.1881	0.10	2725.6	1.6	2725.7	1.77
3A 20.01m	This study	Tuff	z44	0.1948	0.15	2783.4	2.5	2783.4	2.63
3A 20.01m	This study	Tuff	z15	0.1899	0.23	2741.7	3.8	2741.7	3.87
3A 20.01m	This study	Tuff	z23	0.1850	0.10	2698.4	1.7	2698.4	1.87
Imandra lopolith	Amelin et al. (1995)	Intrusion	z38	0.15866	0.16	2441.4	2.7	2441.4	2.82
Imandra lopolith	Amelin et al. (1995)	Intrusion	z39	0.15855	0.11	2440.3	1.8	2440.3	2.03
Imandra lopolith	Amelin et al. (1995)	Intrusion	z40	0.15887	0.11	2443.6	1.9	2443.7	2.03
Imandra lopolith	Amelin et al. (1995)	Intrusion	z41	0.15853	0.07	2440.0	1.2	2440.0	1.43
Seidorechka	Amelin et al. (1995)	Volcanic	z42	0.15793	0.04	2433.6	0.7	2433.6	1.05
Seidorechka	Amelin et al. (1995)	Volcanic	z43	0.15829	0.06	2437.4	1.0	2437.5	1.29
Seidorechka	Amelin et al. (1995)	Volcanic	z44	0.15852	0.11	2439.9	1.9	2439.9	2.03
Seidorechka	Amelin et al. (1995)	Volcanic	z45	0.15824	0.08	2436.9	1.3	2436.9	1.57
Seidorechka	Amelin et al. (1995)	Volcanic	z46	0.15866	0.09	2441.4	1.5	2441.4	1.72
Seidorechka	Amelin et al. (1995)	Volcanic	z47	0.15849	0.07	2439.6	1.1	2439.6	1.43
Seidorechka	Amelin et al. (1995)	Volcanic	z48	0.15859	0.08	2440.7	1.4	2440.7	1.57
Seidorechka	Amelin et al. (1995)	Volcanic	z49	0.15839	0.11	2438.5	1.9	2438.5	2.03

a. Age calculated using $^{207}Pb/^{206}Pb$ ratio and $^{238}U/^{235}U = 137.88$

b. Only considers uncertainty in $^{207}Pb/^{206}Pb$ ratio

c. Age calculated using $^{207}Pb/^{206}Pb$ ratio and $^{238}U/^{235}U = 137.818 \pm 0.045$

d. Combines uncertainty in $^{207}Pb/^{206}Pb$ ratio with uncertainty in $^{238}U/^{235}U$ ratio

Table S4: Summary of interpreted $^{207}Pb/^{206}Pb$ dates and uncertainties related to choice of $^{238}U/^{235}U$ ratio.